

Equalizing excitation–inhibition ratios across visual cortical neurons

Mingshan Xue^{1,2,†}, Bassam V. Atallah³ & Massimo Scanziani^{1,2,4}

The relationship between synaptic excitation and inhibition (E/I ratio), two opposing forces in the mammalian cerebral cortex, affects many cortical functions such as feature selectivity and gain^{1,2}. Individual pyramidal cells show stable E/I ratios in time despite fluctuating cortical activity levels. This is because when excitation increases, inhibition increases proportionally through the increased recruitment of inhibitory neurons, a phenomenon referred to as excitation–inhibition balance^{3–9}. However, little is known about the distribution of E/I ratios across pyramidal cells. Through their highly divergent axons, inhibitory neurons indiscriminately contact most neighbouring pyramidal cells^{10,11}. Is inhibition homogeneously distributed¹² or is it individually matched to the different amounts of excitation received by distinct pyramidal cells? Here we discover that pyramidal cells in layer 2/3 of mouse primary visual cortex each receive inhibition in a similar proportion to their excitation. As a consequence, E/I ratios are equalized across pyramidal cells. This matched inhibition is mediated by parvalbumin-expressing but not somatostatin-expressing inhibitory cells and results from the independent adjustment of synapses originating from individual parvalbumin-expressing cells targeting different pyramidal cells. Furthermore, this match is activity-dependent as it is disrupted by perturbing pyramidal cell activity. Thus, the equalization of E/I ratios across pyramidal cells reveals an unexpected degree of order in the spatial distribution of synaptic strengths and indicates that the relationship between the cortex's two opposing forces is stabilized not only in time but also in space.

To determine the distribution of E/I ratios among layer 2/3 neighbouring pyramidal cells (Fig. 1a), we used adeno-associated virus (AAV) to conditionally express channelrhodopsin-2 (ChR2)^{13–15} in *Scnn1a-Cre-Tg3* mice and photoactivated layer 4 excitatory neurons, one of the main sources of synaptic excitation to layer 2/3, in acute visual cortical slices (Extended Data Fig. 1). We compared the E/I ratios between two to four simultaneously recorded layer 2/3 pyramidal cells (inter-soma distance $39.4 \pm 2.5 \mu\text{m}$, mean \pm s.e.m.; Extended Data Fig. 2) voltage clamped alternatively at the reversal potential for synaptic inhibition and excitation to isolate excitatory postsynaptic currents (EPSCs) and disynaptic inhibitory postsynaptic currents (IPSCs), respectively. EPSC amplitudes greatly varied between simultaneously recorded neurons and so did IPSC amplitudes (Fig. 1b). Despite the heterogeneous distributions of EPSC and IPSC amplitudes among pyramidal cells, however, we found a strong correlation between their amplitudes. That is, neurons with larger EPSCs also received larger IPSCs (Fig. 1c, e). As a consequence, the distribution of E/I ratios across pyramidal cells varied much less than the distributions of EPSC and IPSC amplitudes (Fig. 1d, f) and much less than if EPSCs and IPSCs were randomly paired between cells (Extended Data Fig. 2). These data indicate that E/I ratios are equalized across pyramidal cells.

This equalization could occur if distinct layer 2/3 pyramidal cells each receive inhibition from a ‘private’ set of inhibitory neurons such that the excitatory afferents that more strongly excite a pyramidal cell also more

strongly excite its private inhibitory neurons. However, the two classes of inhibitory neurons, parvalbumin-expressing (Pvalb) and somatostatin-expressing (Sst) cells, that provide most inhibition to layer 2/3 pyramidal

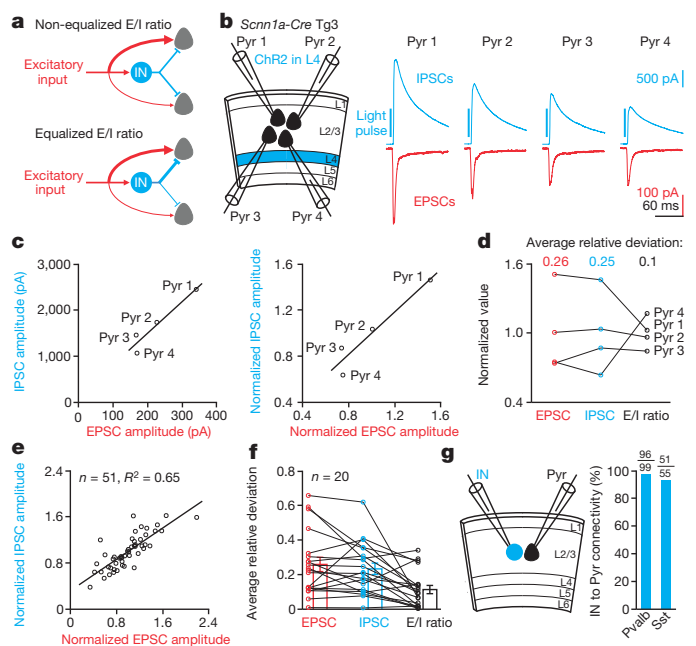


Figure 1 | Equalized E/I ratios across pyramidal cells. **a**, Two alternative models for the spatial distribution of E/I ratios across pyramidal cells. Top, the divergent axons of inhibitory neurons (IN) homogeneously inhibit neighbouring pyramidal cells. Pyramidal cells receiving more excitation have a larger E/I ratio. Bottom, despite divergent axons, inhibitory neurons generate larger inhibition in pyramidal cells receiving more excitation. Accordingly E/I ratios are equalized across pyramidal cells. **b**, Left, schematic of experiments. *Scnn1a-Cre-Tg3* mice with ChR2 in layer 4 excitatory neurons. Right, monosynaptic EPSCs and disynaptic IPSCs from four simultaneously recorded layer 2/3 pyramidal cells (Pyr) in response to layer 4 photoactivation. Note larger IPSCs in neurons receiving larger EPSCs. **c**, EPSC amplitudes of the four neurons in **b** plotted against their IPSC amplitudes. Left, absolute amplitudes. Right, normalized amplitudes. EPSC (or IPSC) amplitudes are normalized by the mean of the simultaneously recorded EPSC (or IPSC) amplitudes. Lines, linear regression fits. **d**, Distributions of normalized EPSC and IPSC amplitudes, and of normalized E/I ratios for the experiment in **b**. E/I ratios are normalized by the mean of the simultaneously recorded ratios. Note narrower distribution of E/I ratios compared with EPSCs or IPSCs. For computing average relative deviations, see Methods. **e**, Summary graphs of normalized EPSCs and IPSCs from 20 similar experiments ($n = 51$ cells). Line, linear regression fit ($R^2 = 0.65$, $P < 0.0001$). **f**, Summary graphs of average relative deviations from 20 similar experiments. Bars, mean \pm s.e.m. The average relative deviations of E/I ratios are 50% smaller than those of EPSCs ($P < 0.0001$) or IPSCs ($P < 0.0001$). **g**, Left, schematic of experiments. Right, connectivity rates from Pvalb and Sst cells to pyramidal cells.

¹Neurobiology Section, Division of Biological Sciences, Center for Neural Circuits and Behavior, University of California, San Diego, La Jolla, California 92093-0634, USA. ²Department of Neuroscience, University of California, San Diego, La Jolla, California 92093-0634, USA. ³Champalimaud Neuroscience Programme, Champalimaud Centre for the Unknown, Lisbon 1400-038, Portugal. ⁴Howard Hughes Medical Institute, University of California, San Diego, La Jolla, California 92093-0634, USA. [†]Present address: Department of Neuroscience, Baylor College of Medicine, Houston, Texas 77030, USA, and Dan Duncan Neurological Research Institute at Texas Children's Hospital, Houston, Texas 77030, USA.

cells showed broad connectivity with pyramidal cells (97% and 93%, respectively, Fig. 1g), as previously shown^{10,11}, thus precluding the private connectivity.

Alternatively, the correlation between excitation and inhibition could be an artefact of the slicing procedure, whereby damaged neurons receive less excitation and less inhibition. To address this possibility we used an independent marker to identify neurons receiving more excitation. We used mice in which the promoter of the activity-dependent immediate early gene *Fos* drives the expression of *Fos* fused to the enhanced green fluorescent protein (*Fos-EGFP*), because in these mice $EGFP^+$ neurons receive more excitation than $EGFP^-$ neurons¹⁶. $EGFP^+$ neurons were predominantly pyramidal cells (Extended Data Fig. 3). We photostimulated layer 4 in acute slices from *Fos-EGFP*, *Scnn1a-Cre-Tg3* mice and simultaneously recorded pairs of $EGFP^+$ and nearby $EGFP^-$ layer 2/3 pyramidal cells. Layer 4 activation generated larger EPSCs in $EGFP^+$ neurons in 78% of all recorded pairs, and $EGFP^+$ neurons received, on average, 40% larger EPSCs (Fig. 2a, b) (the average logarithm of $EGFP^+/EGFP^-$ ratios was 0.15). Importantly, $EGFP^+$ neurons also received larger disynaptic IPSCs (Fig. 2a, c). Consequently, the E/I ratios of $EGFP^+$ and $EGFP^-$ neurons were similar (Fig. 2d).

Taken together, these results demonstrate that excitation and inhibition, despite varying in amplitudes between pyramidal cells, remain proportional to each other, thus equalizing E/I ratios.

Which type of interneuron provides the inhibition that matches layer-4-mediated excitation? We took advantage of the fact that $EGFP^+$ neurons in *Fos-EGFP* mice receive larger excitation from layer 4 and crossed them to *Pvalb-ires-Cre* or *Sst-ires-Cre* mice to express ChR2 conditionally. Photoactivation of Pvalb cells generated larger monosynaptic IPSCs in $EGFP^+$ than in $EGFP^-$ neurons (Fig. 2e, f). In contrast, Sst cells generated IPSCs whose amplitudes did not correlate with EGFP expression (Fig. 2g, h). These data indicate that Pvalb cells, but not Sst cells, provide stronger inhibition onto neurons that receive stronger layer-4-mediated excitation, thereby contributing to the equalization of E/I ratios.

What mechanism regulates the strengths of excitation and/or inhibition to achieve the observed proportionality? Excitation and inhibition may reach their specific ratio by using the pyramidal cell's activity as a measure of their relative strengths. For example, the low activity caused by a strong Pvalb-cell-mediated inhibition or by a weak layer-4-mediated excitation could be the signal to increase layer-4-mediated excitation or to decrease Pvalb-cell-mediated inhibition, respectively, until a neuron's specific higher set-point activity is reached. In both possibilities the initially small E/I ratio is increased by either increasing excitation to match the large inhibition or by decreasing inhibition to match the small excitation. Both possibilities are plausible since the activity of individual neurons can regulate the strengths of both excitatory and inhibitory synapses^{17–20}. If this hypothesis is correct, perturbing the activity of pyramidal cells should disrupt the proportionality between excitation and inhibition. For example, reducing the excitability of a pyramidal cell should increase its E/I ratio by either increasing excitation (the first possibility), or decreasing inhibition (the second possibility), or both.

We reduced the excitability of a small, random subset of layer 2/3 pyramidal cells in primary visual cortex (V1) by overexpressing a Kir2.1 channel via *in utero* electroporation (IUE)^{21–23} (Fig. 3a). Recordings in acute slices confirmed the reduced excitability in Kir2.1-overexpressing cells (Kir2.1 neurons) compared with untransfected control pyramidal cells (Extended Data Fig. 4). *In vivo* targeted recordings from Kir2.1 and nearby control neurons (Fig. 3b, c) demonstrated that Kir2.1 overexpression drastically suppressed visual-evoked and spontaneous activity (Fig. 3d–f). We then examined the impact of this perturbation on excitation and inhibition. We photostimulated layer 4 and simultaneously recorded Kir2.1 and neighbouring control neurons in the acute slices from *Scnn1a-Cre-Tg3* mice. Surprisingly, layer-4-mediated excitation was not significantly different between these two groups (Fig. 3g, h), invalidating the first aforementioned possibility. In contrast, disynaptic inhibition was significantly smaller in Kir2.1 neurons (Fig. 3g, i),

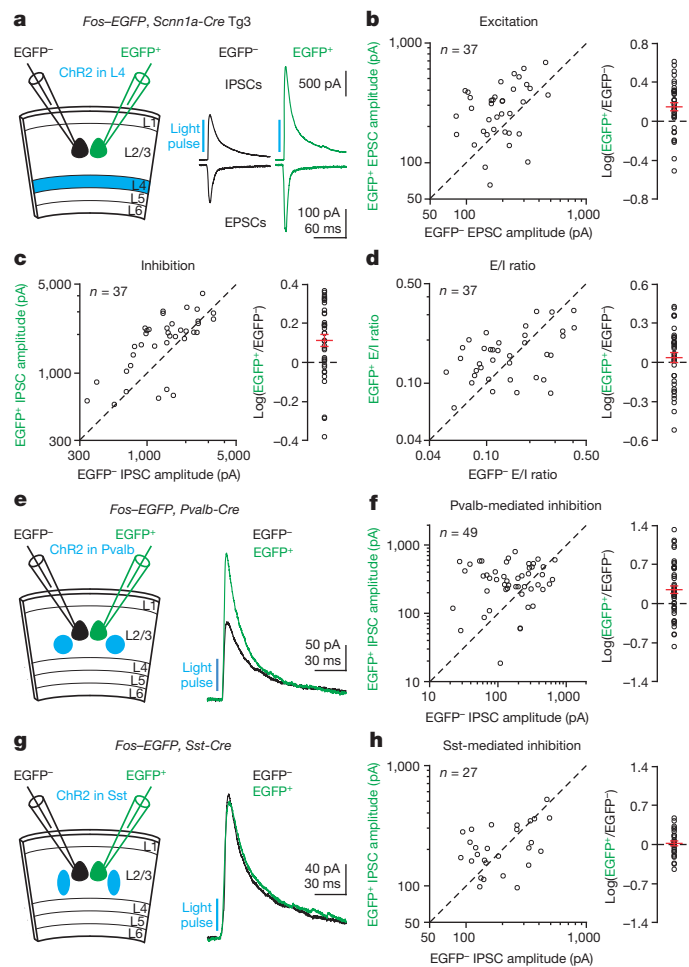


Figure 2 | Pvalb-cell-mediated inhibition matches layer-4-mediated excitation. **a**, Left, schematic of experiments. *Fos-EGFP*, *Scnn1a-Cre-Tg3* mice with ChR2 in layer 4 excitatory neurons. Right, monosynaptic EPSCs and disynaptic IPSCs from simultaneously recorded $EGFP^-$ and $EGFP^+$ neurons in response to layer 4 photoactivation. Note larger synaptic currents in $EGFP^+$ neuron. **b–d**, Summary graphs of 37 similar experiments. **b**, Left, EPSC amplitudes in $EGFP^+$ neurons plotted against those in $EGFP^-$ neurons. Right, logarithm of the ratio between EPSC amplitudes in $EGFP^+$ and $EGFP^-$ neurons. Red, mean \pm s.e.m. EPSC amplitudes are 40% larger in $EGFP^+$ neurons ($P = 0.0004$). **c**, As in **b**, but for disynaptic IPSCs. Disynaptic IPSC amplitudes are 30% larger in $EGFP^+$ neurons ($P = 0.001$). **d**, As in **b**, but for E/I ratios. E/I ratios are similar between $EGFP^+$ and $EGFP^-$ neurons ($P = 0.7$). **e**, Left, schematic of experiments. *Fos-EGFP*, *Pvalb-ires-Cre* mice with ChR2 in Pvalb cells. Right, IPSCs from simultaneously recorded $EGFP^-$ and $EGFP^+$ neurons in response to Pvalb cell photoactivation. Note larger IPSC in $EGFP^+$ neuron. **f**, Summary graph. Left, IPSC amplitudes in $EGFP^+$ neurons plotted against those in $EGFP^-$ neurons. Right, logarithm of the ratio between IPSC amplitudes in $EGFP^+$ and $EGFP^-$ neurons. Red, mean \pm s.e.m. IPSC amplitudes are 77% larger in $EGFP^+$ neurons ($n = 49$, $P = 0.001$). **g**, **h**, As in **e**, **f**, but for *Fos-EGFP*, *Sst-ires-Cre* mice with ChR2 in Sst cells. IPSC average amplitudes are similar between $EGFP^+$ and $EGFP^-$ neurons ($n = 27$, $P = 0.7$).

consistent with the second possibility. The effect on inhibition was due to the channel function of Kir2.1 because a non-conducting Kir2.1 mutant (Extended Data Fig. 4) had no effect (Extended Data Fig. 5). Thus, perturbing layer 2/3 pyramidal cell excitability disrupts the proportionality between excitation and inhibition (Fig. 3j). These data indicate that pyramidal cell activity contributes to the equalization of E/I ratios across pyramidal cells.

If pyramidal cell activity contributes to establishing the proportionality between layer-4-mediated excitation and Pvalb-cell-mediated inhibition, then the decrease in excitability should selectively decrease

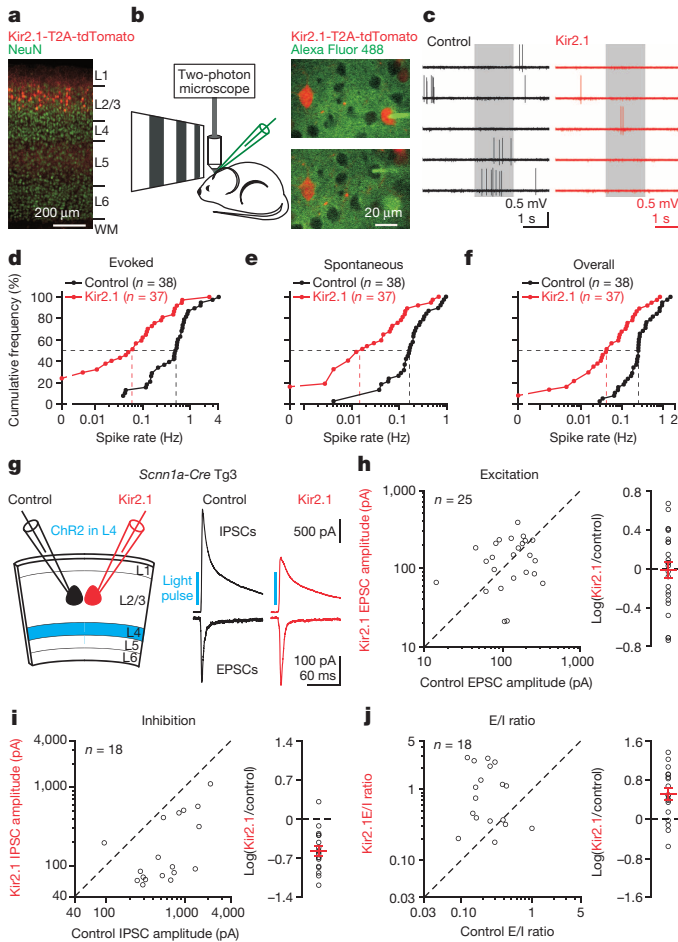


Figure 3 | Suppressing pyramidal cell activity reduces inhibition but not excitation. **a**, Fluorescent image of a V1 coronal section showing Kir2.1-T2A-tdTomato overexpression in a small subset of layer 2/3 pyramidal cells ($9 \pm 1\%$, mean \pm s.e.m., $n = 12$ sections from six mice). Cortical layers are identified by NeuN staining. L, layer, WM, white matter. **b**, Left, schematic of *in vivo* experiments. Right, a Kir2.1 neuron (upper panel) and a control neuron (lower panel) were sequentially recorded with Alexa Fluor 488-filled pipettes. **c**, Recordings from a control and a Kir2.1 neuron show spontaneous and visual-evoked spikes. Grey box, visual stimulation period. Note reduced spiking in Kir2.1 neuron. **d–f**, Cumulative frequencies of evoked spike rate (**d**, median: control, 0.50 Hz; Kir2.1, 0.061 Hz; $P < 0.0001$), spontaneous spike rate (**e**, median: control, 0.16 Hz; Kir2.1, 0.017 Hz; $P < 0.0001$) and overall spike rate (**f**, median: control, 0.25 Hz; Kir2.1, 0.043 Hz; $P < 0.0001$) from 38 control neurons and 37 Kir2.1 neurons. **g**, Left, schematic of slice experiments. *Scnn1a-Cre-Tg3* mice with Chr2 in layer 4 excitatory neurons and Kir2.1 in a subset of layer 2/3 pyramidal cells. Right, monosynaptic EPSCs and disynaptic IPSCs from simultaneously recorded control and Kir2.1 neurons in response to layer 4 photoactivation. Note similar EPSC but smaller disynaptic IPSC in Kir2.1 neuron compared with control neuron. **h–j**, Summary graphs. **h**, Left, EPSC amplitudes in Kir2.1 neurons plotted against those in control neurons. Right, logarithm of the ratio between EPSC amplitudes in Kir2.1 and control neurons. Red, mean \pm s.e.m. EPSC average amplitudes are similar between Kir2.1 and control neurons ($n = 25$, $P = 0.8$). **i**, As in **h**, but for disynaptic IPSCs. Disynaptic IPSC amplitudes in Kir2.1 neurons are 27% of those in control neurons ($n = 18$, $P = 0.0003$). **j**, As in **h**, but for E/I ratios. E/I ratios in Kir2.1 neurons are threefold those in control neurons ($n = 18$, $P = 0.004$).

Pvalb- but not Sst-cell-mediated inhibition. Conversely, an increase in excitability should selectively increase Pvalb-cell-mediated inhibition. Indeed, Pvalb-cell-mediated inhibition was significantly smaller in Kir2.1 than in control neurons, whereas Sst-cell-mediated inhibition was similar (Fig. 4a–e). Overexpression of the non-conducting Kir2.1 mutant did not affect Pvalb-cell-mediated inhibition (Extended Data Fig. 5). We used a bacterial voltage-gated Na^+ channel (mNaChBac) to enhance neuronal excitability. Neurons expressing mNaChBac generate

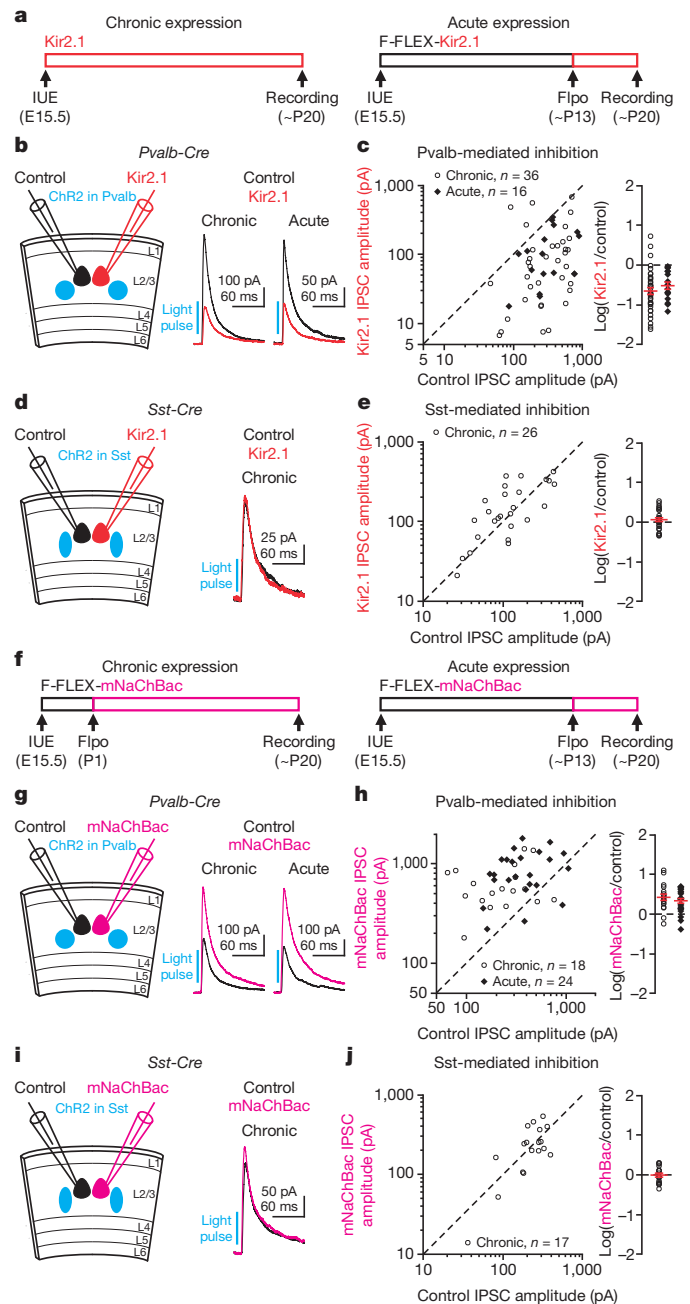


Figure 4 | Bidirectional regulation of Pvalb- but not Sst-cell-mediated inhibition. **a**, Schematic of chronic and acute expression of Kir2.1. Red bars, approximate Kir2.1 expression time course. **b**, Left, schematic of experiments. *Pvalb-ires-Cre* mice with Chr2 in Pvalb cells and Kir2.1 in a subset of layer 2/3 pyramidal cells. Right, IPSCs from simultaneously recorded control neuron and neuron chronically or acutely expressing Kir2.1 in response to Pvalb cell photoactivation. Note smaller IPSCs in Kir2.1 neuron. **c**, Summary graphs. Left, IPSC amplitudes in Kir2.1 neurons plotted against those in control neurons. Right, logarithm of the ratio between IPSC amplitudes in Kir2.1 and control neurons. Red, mean \pm s.e.m. IPSC amplitudes in Kir2.1 neurons are 23% ($n = 36$, $P < 0.0001$) and 31% ($n = 16$, $P = 0.0005$) of those in control neurons for chronic and acute conditions, respectively. **d**, **e**, As in **b**, **c**, but for *Sst-ires-Cre* mice with Chr2 in *Sst* cells and Kir2.1 chronically in a subset of layer 2/3 pyramidal cells. On average IPSC amplitudes are similar between Kir2.1 and control neurons ($n = 26$, $P = 0.3$). **f**, Schematic of chronic and acute expression of mNaChBac. Magenta bars, approximate mNaChBac expression time course. **g**, **h**, As in **b**, **c**, but for mNaChBac. IPSC amplitudes in mNaChBac neurons are 2.7-fold ($n = 18$, $P = 0.001$) and 2.2-fold ($n = 24$, $P = 0.0003$) those in control neurons for chronic and acute conditions, respectively. **i**, **j**, As in **d**, **e**, but for mNaChBac. On average, IPSC amplitudes are similar between mNaChBac and control neurons ($n = 17$, $P = 0.7$).

long-lasting action potentials and depolarization of the order of hundreds of milliseconds (Extended Data Fig. 6). Because constitutive expression of mNaChBac in cortical neurons from embryonic day 15.5 (E15.5) caused a neuronal migration defect (Extended Data Fig. 7), we devised a Flpo recombinase-mediated flip-excision strategy, F-FLEX switch (Extended Data Fig. 8), to conditionally express mNaChBac postnatally. We combined *in utero* electroporation of a Flpo-dependent mNaChBac-expressing plasmid, to randomly transfect a small subset of layer 2/3 pyramidal cells, with injection of an AAV expressing Flpo at postnatal day 1 (P1), to turn on mNaChBac expression. This allowed us to concurrently express ChR2 in Pvalb or Sst cells, and mNaChBac in layer 2/3 pyramidal cells without affecting their migration (Extended Data Fig. 7). Pvalb-cell-mediated inhibition was significantly larger in mNaChBac neurons than in control neurons (Fig. 4f–h), and a non-conducting mNaChBac mutant (Extended Data Fig. 6) had no effect (Extended Data Fig. 5). mNaChBac expression did not alter Sst-cell-mediated inhibition (Fig. 4i, j). To determine whether also more acute perturbations of layer 2/3 pyramidal cell excitability alter Pvalb-cell-mediated inhibition, we used Flpo and F-FLEX switch to express Kir2.1 or mNaChBac for only approximately 1 week starting around postnatal days 12–14. This acute decrease (Kir2.1) or increase (mNaChBac) in excitability caused a decrease or an increase in Pvalb-cell-mediated inhibition, respectively, similar to the changes caused by the chronic expression of Kir2.1 or mNaChBac (Fig. 4a–c, f–h). These data indicate that the proportionality between layer-4-mediated excitation and Pvalb-cell-mediated inhibition is equalized across pyramidal cells through the bidirectional modulation of the strength of Pvalb cell synapses.

The above results show that the spatial heterogeneity of Pvalb-cell-mediated inhibition ensures the equalization of E/I ratios across pyramidal cells. Is the inhibition mediated by a single Pvalb cell also heterogeneous across its targeted pyramidal cells? We first determined whether the relative amplitudes of unitary IPSCs (uIPSCs) mediated by a Pvalb cell onto its targets are predicted by the relative activity of these targets. We suppressed the activity of a small subset of layer 2/3 pyramidal cells by overexpressing Kir2.1 and simultaneously recorded from a layer 2/3 Pvalb cell, a control and a Kir2.1 neuron (Fig. 5a). Although the Pvalb-to-pyramidal cell connectivity was similarly high, regardless of whether pyramidal cells overexpressed Kir2.1 (Fig. 5f), uIPSC amplitude was significantly smaller in Kir2.1 neurons than in control neurons (Fig. 5b, f). All properties of the unitary connections between Pvalb cells and control neurons were similar to those recorded in mice that were not transfected with Kir2.1 (Extended Data Fig. 9), indicating a cell-autonomous effect of Kir2.1 overexpression. We assessed the variability of uIPSC amplitudes originating from a single Pvalb cell and determined its dependency on the activity of the targeted pyramidal cells. We simultaneously recorded from a layer 2/3 Pvalb cell and two or three nearby pyramidal cells that were either all control or all Kir2.1 neurons (Fig. 5c, d). uIPSC amplitudes varied greatly from one control neuron to another, but less among Kir2.1 neurons (Fig. 5c–e, g), possibly because suppressing pyramidal cell activity cannot reduce uIPSC amplitudes below a certain level (flooring effect) (Extended Data Fig. 10). Thus, the inhibition generated by even an individual Pvalb cell onto its targets is remarkably heterogeneous, and this heterogeneity reflects in part the activity profile of the targeted pyramidal cell population. Hence, despite the indiscriminate connectivity of Pvalb cells, the amount of inhibition that they provide onto each of their targets is adjusted to equalize the E/I ratios (Fig. 5h).

Both theoretical and experimental evidence indicates that the relationship between synaptic excitation and inhibition in the cerebral cortex is fundamental for sensory processing^{1,2,24–27}. Failure to establish or maintain this relationship may be the neural basis of neurological disorders such as schizophrenia and autism^{28,29}. We discover that E/I ratios are remarkably similar across different pyramidal cells despite large variations in the amplitudes of synaptic excitation and inhibition. The activity-dependent adjustment of inhibition to match excitation may result from activity-dependent gene expression^{19,20,30}. Our study provides insight into how two opposing synaptic inputs, layer-4-mediated

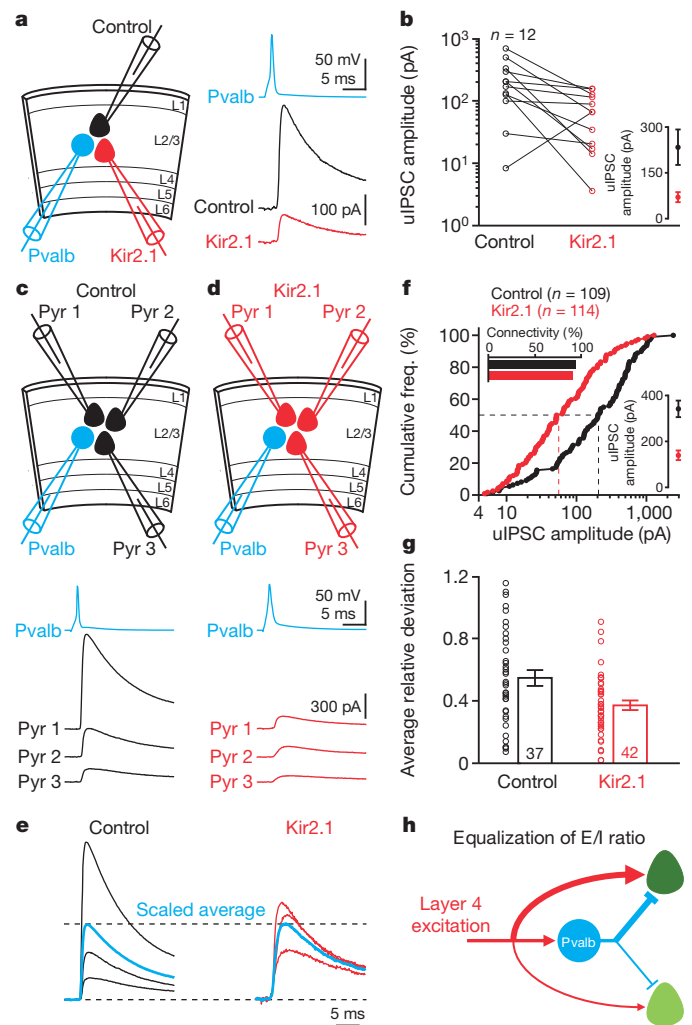


Figure 5 | Inhibition mediated by individual Pvalb cells varies depending on targets' activity. **a**, Left, schematic of experiments. Right, uIPSCs from simultaneously recorded control and Kir2.1 neuron in response to an action potential in a Pvalb cell. Note smaller uIPSC in Kir2.1 neuron. **b**, Summary graphs of uIPSC amplitudes from 12 similar experiments ($P = 0.005$). Inset, mean \pm s.e.m. **c**, Top, schematic of experiments. Bottom, uIPSCs simultaneously recorded from three control neurons in response to an action potential in a Pvalb cell. **d**, As in **c**, but for three Kir2.1 neurons. **e**, The uIPSCs from **c** and **d** were normalized by their respective mean amplitudes (scaled average). Note larger inter-cell variability of uIPSCs among control neurons. **f**, Cumulative frequencies of uIPSC amplitudes (control: $n = 109$, median, 205.4 pA; Kir2.1: $n = 114$, 57.4 pA; $P < 0.0001$). Lower inset, mean \pm s.e.m. of uIPSC amplitudes. Upper inset, unitary connectivity rates from Pvalb cells to control (109 out of 116) and Kir2.1 (114 out of 126) neurons are similar ($P = 0.3$). **g**, Summary graph for the average relative deviations of uIPSCs from 37 and 42 experiments as in **c** and **d**. Bars, mean \pm s.e.m. The average relative deviations for Kir2.1 neurons are 33% smaller than those for control neurons ($P = 0.009$). **h**, Schematic of the equalized E/I ratios across cortical neurons.

excitation and Pvalb-cell-mediated inhibition, remain proportional across a population of pyramidal cells. Thus it reveals an unanticipated degree of order in the distribution of synaptic strengths in cortical space.

METHODS SUMMARY

Cre-dependent recombinant AAV vectors were injected postnatally into Cre-expressing mice to conditionally express ChR2. Plasmids were electroporated *in utero* at embryonic day 14.5 or 15.5 to transfect a small, random subset of layer 2/3 pyramidal cells. For *in vitro* physiology, mice at postnatal days 14–23 were anaesthetized and transcardially perfused. Coronal slices were perfused with artificial cerebrospinal fluid for whole-cell recordings at 31–32 °C. A light-emitting diode (470 nm) was used to deliver blue light to stimulate neurons via the activation of

ChR2. For *in vivo* physiology, mice at postnatal days 17–23 were anaesthetized by intraperitoneal injection of chlorprothixene (5 mg kg⁻¹) followed by urethane (1.2 g kg⁻¹) and the body temperature was maintained at 37 °C. A craniotomy at V1 was performed and targeted loose-patch recordings were performed under the guidance of two-photon laser scanning microscopy.

Online Content Methods, along with any additional Extended Data display items and Source Data, are available in the online version of the paper; references unique to these sections appear only in the online paper.

Received 2 January; accepted 8 April 2014.

Published online 22 June 2014.

- Haider, B. & McCormick, D. A. Rapid neocortical dynamics: cellular and network mechanisms. *Neuron* **62**, 171–189 (2009).
- Isaacson, J. S. & Scanziani, M. How inhibition shapes cortical activity. *Neuron* **72**, 231–243 (2011).
- Anderson, J. S., Carandini, M. & Ferster, D. Orientation tuning of input conductance, excitation, and inhibition in cat primary visual cortex. *J. Neurophysiol.* **84**, 909–926 (2000).
- Shu, Y., Hasenstaub, A. & McCormick, D. A. Turning on and off recurrent balanced cortical activity. *Nature* **423**, 288–293 (2003).
- Wehr, M. & Zador, A. M. Balanced inhibition underlies tuning and sharpens spike timing in auditory cortex. *Nature* **426**, 442–446 (2003).
- Wilent, W. B. & Contreras, D. Synaptic responses to whisker deflections in rat barrel cortex as a function of cortical layer and stimulus intensity. *J. Neurosci.* **24**, 3985–3998 (2004).
- Haider, B., Duque, A., Hasenstaub, A. R. & McCormick, D. A. Neocortical network activity *in vivo* is generated through a dynamic balance of excitation and inhibition. *J. Neurosci.* **26**, 4535–4545 (2006).
- Okun, M. & Lampl, I. Instantaneous correlation of excitation and inhibition during ongoing and sensory-evoked activities. *Nature Neurosci.* **11**, 535–537 (2008).
- Atallah, B. V. & Scanziani, M. Instantaneous modulation of gamma oscillation frequency by balancing excitation with inhibition. *Neuron* **62**, 566–577 (2009).
- Fino, E. & Yuste, R. Dense inhibitory connectivity in neocortex. *Neuron* **69**, 1188–1203 (2011).
- Packer, A. M. & Yuste, R. Dense, unspecific connectivity of neocortical parvalbumin-positive interneurons: a canonical microcircuit for inhibition? *J. Neurosci.* **31**, 13260–13271 (2011).
- Pouille, F., Marin-Burgin, A., Adesnik, H., Atallah, B. V. & Scanziani, M. Input normalization by global feedforward inhibition expands cortical dynamic range. *Nature Neurosci.* **12**, 1577–1585 (2009).
- Nagel, G. *et al.* Channelrhodopsin-2, a directly light-gated cation-selective membrane channel. *Proc. Natl Acad. Sci. USA* **100**, 13940–13945 (2003).
- Boyden, E. S., Zhang, F., Bamberg, E., Nagel, G. & Deisseroth, K. Millisecond-timescale, genetically targeted optical control of neural activity. *Nature Neurosci.* **8**, 1263–1268 (2005).
- Li, X. *et al.* Fast noninvasive activation and inhibition of neural and network activity by vertebrate rhodopsin and green algae channelrhodopsin. *Proc. Natl Acad. Sci. USA* **102**, 17816–17821 (2005).
- Benedetti, B. L., Takashima, Y., Wen, J. A., Urban-Ciecko, J. & Barth, A. L. Differential wiring of layer 2/3 neurons drives sparse and reliable firing during neocortical development. *Cereb. Cortex* **23**, 2690–2699 (2013).
- Burrone, J., O'Byrne, M. & Murthy, V. N. Multiple forms of synaptic plasticity triggered by selective suppression of activity in individual neurons. *Nature* **420**, 414–418 (2002).
- Ibata, K., Sun, Q. & Turrigiano, G. G. Rapid synaptic scaling induced by changes in postsynaptic firing. *Neuron* **57**, 819–826 (2008).
- Peng, Y. R. *et al.* Postsynaptic spiking homeostatically induces cell-autonomous regulation of inhibitory inputs via retrograde signaling. *J. Neurosci.* **30**, 16220–16231 (2010).
- Sim, S., Antolin, S., Lin, C. W., Lin, Y. X. & Lois, C. Increased cell-intrinsic excitability induces synaptic changes in new neurons in the adult dentate gyrus that require npas4. *J. Neurosci.* **33**, 7928–7940 (2013).
- Saito, T. & Nakatsuji, N. Efficient gene transfer into the embryonic mouse brain using *in vivo* electroporation. *Dev. Biol.* **240**, 237–246 (2001).
- Tabata, H. & Nakajima, K. Efficient *in utero* gene transfer system to the developing mouse brain using electroporation: visualization of neuronal migration in the developing cortex. *Neuroscience* **103**, 865–872 (2001).
- Hatanaka, Y., Hisanaga, S., Heizmann, C. W. & Murakami, F. Distinct migratory behavior of early- and late-born neurons derived from the cortical ventricular zone. *J. Comp. Neurol.* **479**, 1–14 (2004).
- van Vreeswijk, C. & Sompolinsky, H. Chaos in neuronal networks with balanced excitatory and inhibitory activity. *Science* **274**, 1724–1726 (1996).
- Vogels, T. P. & Abbott, L. F. Gating multiple signals through detailed balance of excitation and inhibition in spiking networks. *Nature Neurosci.* **12**, 483–491 (2009).
- Renart, A. *et al.* The asynchronous state in cortical circuits. *Science* **327**, 587–590 (2010).
- Vogels, T. P., Sprekeler, H., Zenke, F., Clopath, C. & Gerstner, W. Inhibitory plasticity balances excitation and inhibition in sensory pathways and memory networks. *Science* **334**, 1569–1573 (2011).
- Rubenstein, J. L. & Merzenich, M. M. Model of autism: increased ratio of excitation/inhibition in key neural systems. *Genes Brain Behav.* **2**, 255–267 (2003).
- Lewis, D. A., Curley, A. A., Glausier, J. R. & Volk, D. W. Cortical parvalbumin interneurons and cognitive dysfunction in schizophrenia. *Trends Neurosci.* **35**, 57–67 (2012).
- Bloodgood, B. L., Sharma, N., Browne, H. A., Trepman, A. Z. & Greenberg, M. E. The activity-dependent transcription factor NPAS4 regulates domain-specific inhibition. *Nature* **503**, 121–125 (2013).

Acknowledgements We thank M. Chan, J. Evora, A. Linder and P. Abelkop for technical assistance; M. S. Caudill and S. R. Olsen for help with the *in vivo* physiology recording programme; E. Kim and A. Ghosh for pCAG-Kir2.1-T2A-tdTomato plasmid; J. Isaacson and H. Y. Zoghbi for comments on earlier versions of the manuscript; D. N. Hill, G. I. Allen, E. Arias-Castro and M. Wang for advice on statistical analysis; the members of the Scanziani and Isaacson laboratories for suggestions; and the University of California, San Diego Neuroscience Microscopy Facility (P30 NS047101) for imaging equipment. M.X. was supported by a fellowship from Jane Coffin Childs Memorial Fund for Medical Research. M.S. is an investigator of the Howard Hughes Medical Institute. This work was also supported by the Gatsby Charitable Foundation.

Author Contributions M.X. and M.S. designed the study. M.X. performed all experiments and data analysis. B.V.A. contributed to data analysis. M.X. and M.S. wrote the manuscript.

Author Information Reprints and permissions information is available at www.nature.com/reprints. The authors declare no competing financial interests. Readers are welcome to comment on the online version of the paper. Correspondence and requests for materials should be addressed to M.X. (mingshanxue@gmail.com) or M.S. (massimo@ucsd.edu).

METHODS

Mice. All procedures to maintain and use mice were approved by the Institutional Animal Care and Use Committee at the University of California, San Diego. Mice were maintained on a reverse 12-h:12-h light:dark cycle with regular mouse chow and water *ad libitum*. CD-1 mice were purchased from Charles River Laboratories or Harlan Laboratories. *Scnn1a-Cre-Tg3* (ref. 31), *Fos-EGFP³²*, *Gad2-ires-Cre³³*, *Pvalb-ires-Cre³⁴*, *Sst-ires-Cre³⁵* and *Rosa-CAG-LSL-tdTomato-WPRE³¹* mice were obtained from the Jackson Laboratory (stock numbers 009613, 014135, 010802, 008069, 013044 and 007909, respectively). Hemizygous transgenic mice and heterozygous knock-in mice of both sexes were used in the experiments.

DNA constructs and transfection of HEK cells. Two point mutations E224G and Y242F were introduced into mouse wild-type Kir2.1 (Kcnj2) to enhance its ability to suppress neuronal activity. Mutation E224G attenuates the Mg²⁺ and polyamine block of Kir2.1 to reduce its inward rectification³⁵. Mutation Y242F blocks tyrosine kinase phosphorylation of Kir2.1 at residue Y242 to enhance its plasma membrane surface expression³⁶. Three point mutations, G144A, Y145A and G146A, were introduced to generate a non-conducting channel³⁷. A Myc tag (EQLKISEEDL) was fused to the amino (N) termini of Kir2.1 E224G Y242F and Kir2.1 E224G Y242F G144A Y145A G146A, referred to as Kir2.1 and Kir2.1Mut, respectively. Both Kir2.1 and Kir2.1Mut were carboxy (C)-terminally fused with a T2A sequence (GSGEGRGSLLTCGDVEENPGP) followed by a tdTomato. The resulting constructs were then cloned into a plasmid containing a CAG promoter (pCAG) to generate pCAG-Kir2.1-T2A-tdTomato and pCAG-Kir2.1Mut-T2A-tdTomato.

The complementary DNA (cDNA) encoding a wild-type bacterial Na⁺ channel NaChBac³⁸ was synthesized *de novo* and codon-optimized for mammalian expression (referred as mNaChBac) by DNA2.0. A point mutation E191K was introduced to generate a non-conducting channel³⁹, referred as mNaChBacMut. Both mNaChBac and mNaChBacMut were C-terminally fused with T2A-tdTomato and cloned into the pCAG plasmid to create pCAG-mNaChBac-T2A-tdTomato and pCAG-mNaChBacMut-T2A-tdTomato, respectively.

F-FLEX cassette using two wild-type Frt sites and two F14 sites⁴⁰ (Extended Data Fig. 8) was synthesized *de novo* and cloned into the plasmid pJ244 by DNA2.0 to generate pJ244-F-FLEX. mNaChBac-T2A-tdTomato and mNaChBacMut-T2A-tdTomato were subcloned into pJ244-F-FLEX in the inverted orientation. F-FLEX-mNaChBac-T2A-tdTomato and F-FLEX-mNaChBacMut-T2A-tdTomato cassettes were then subcloned into an AAV *cis*-plasmid containing an EF1 α promoter to generate pAAV-EF1 α -F-FLEX-mNaChBac-T2A-tdTomato and pAAV-EF1 α -F-FLEX-mNaChBacMut-T2A-tdTomato, respectively. mNaChBac-T2A-tdTomato in pAAV-EF1 α -F-FLEX-mNaChBac-T2A-tdTomato was replaced with inverted Kir2.1-T2A-tdTomato to generate pAAV-EF1 α -F-FLEX-Kir2.1-T2A-tdTomato.

An improved version of Flp recombinase, Flpo⁴¹ was cloned into a pCAG plasmid and an AAV *cis*-plasmid containing a human synapsin promoter to generate pCAG-Flpo and pAAV-hSynapsin-Flpo, respectively. pCAG-EGFP⁴², pCAG-mRFP⁴³ and pCAG-Cre⁴⁴ were obtained from Addgene (11150, 28311 and 13775, respectively).

HEK-293FT cells (Life Technologies) were transfected with DNA constructs (0.1–0.5 μ g) in 12-well plates using Lipofectamine 2000 (Life Technologies) to test their functionality. The following constructs were used in Extended Data Fig. 8c, d: pCAG-EGFP, pCAG-mRFP, pCAG-Flpo, pCAG-Cre, pAAV-EF1 α -F-FLEX-mNaChBac-T2A-tdTomato and pAAV-EF1 α -DIO-hChR2(H134R)-EYFP.

In utero electroporation. Female CD-1 mice were crossed with male *Scnn1a-Cre-Tg3*, *Pvalb-ires-Cre*, or *Sst-ires-Cre* mice to obtain timed pregnancies. pCAG-Kir2.1-T2A-tdTomato, pCAG-Kir2.1Mut-T2A-tdTomato, pCAG-mNaChBac-T2A-tdTomato, and pCAG-mNaChBacMut-T2A-tdTomato were used at the final concentrations of 2–3 μ g μ l⁻¹. pAAV-EF1 α -F-FLEX-mNaChBac-T2A-tdTomato, pAAV-EF1 α -F-FLEX-mNaChBacMut-T2A-tdTomato or pAAV-EF1 α -F-FLEX-Kir2.1-T2A-tdTomato (2–3 μ g μ l⁻¹ final concentration) was mixed with pCAG-EGFP (0.2 μ g μ l⁻¹ final concentration). Fast Green (Sigma-Aldrich, 0.01% final concentration) was added to the DNA solution. On embryonic day 14.5 or 15.5, female mice were anaesthetized with 2.5% isoflurane in oxygen at a flow rate of 1 l min⁻¹ and the body temperature was maintained by a feedback-based DC temperature control system (FHC) at 37 °C. Buprenorphine (3 μ g, Reckitt Benckiser Healthcare) was administered subcutaneously along with 1 ml of Lactated Ringer's Injection (Baxter Healthcare). The abdominal fur was shaved and the skin was cleaned with 70% alcohol and iodine. A sterile towel drape was laid on the mouse with only the abdomen exposed. Midline incisions (2 cm) were made on the abdominal skin and wall, and the uteri were taken out of the abdominal cavity. A bevelled glass micropipette (tip size 100- μ m outer diameter, 50- μ m inner diameter) was used to penetrate the uterus and the embryo skull to inject about 1.5 μ l of DNA solution into one lateral ventricle. Five pulses of current (voltage 39 V, duration 50 ms) were delivered at 1 Hz with a Tweezertrode (5-mm diameter) and a square-wave pulse generator (ECM 830, BTX Harvard Apparatus). The electrode paddles were positioned along the 70° angle to the brain's sagittal plane. The cathode faced the occipital side of the injected ventricle to target the visual cortex. After electroporation, uteri were put back into the

abdominal cavity, and the abdominal wall and skin were sutured. Mice were returned to the home cage and recovered from anaesthesia on a 37 °C Deltaphase Isothermal Pad (Braintree Scientific). Additional buprenorphine (3 μ g) was administered subcutaneously on the next day. After birth, transfected pups were identified by the transcranial fluorescence of tdTomato or EGFP with a stereomicroscope (MVX10 Macroview, Olympus). Only the pups in which the majority of the transfection occurred in the primary visual cortex were used for experiments.

AAV production and injection. All recombinant AAV vectors were produced by the Penn Vector Core with the following titres: AAV2/9-CAGGS-Flex-ChR2-tdTomato⁴⁵ (Addgene 18917, titre 1.15 \times 10¹³ genome copies per millilitre), AAV2/1-CAGGS-Flex-ChR2-tdTomato (titre 6.86 \times 10¹² or 1.22 \times 10¹³ genome copies per millilitre), AAV2/9-EF1 α -DIO-hChR2(H134R)-EYFP⁴⁶ (Addgene 20298, titre 6.24 \times 10¹² or 1.18 \times 10¹³ genome copies per millilitre), AAV2/1-EF1 α -DIO-hChR2(H134R)-EYFP (titre 3.41 \times 10¹³ genome copies per millilitre) and AAV2/9-hSynapsin-Flpo (titre 1.57 \times 10¹³ genome copies per millilitre).

Injection at postnatal days 0–2. AAV was injected into the V1 of pups using a Nanoject II nanolitre injector (Drummond Scientific Company). Pups were anaesthetized by hypothermia and secured on a custom-made plate. Fast Green (0.01% final concentration) was added to the virus solution for visualization. A bevelled glass micropipette (tip size 60- μ m outer diameter, 30- μ m inner diameter) was used to penetrate the scalp and skull, and to inject AAV at different depths (600, 500, 400 and 300 μ m below the scalp) of one location (1.6 mm lateral and 0.3 mm caudal from the lambda). A total of about 80–180 nl (adjusted based on the virus titres) of virus solution was injected over 60 s. After injection, the micropipette was kept in the parenchyma at 300- μ m depth for 30 s before being slowly withdrawn. Pups were placed on a 37 °C Deltaphase Isothermal Pad to recover from anaesthesia and then were returned to the dam. For chronic expression of mNaChBac or mNaChBacMut, a mix of AAV2/9-hSynapsin-Flpo (titre 1.57 \times 10¹³ genome copies per millilitre) and AAV2/9-EF1 α -DIO-hChR2(H134R)-EYFP (titre 1.18 \times 10¹³ genome copies per millilitre) at a ratio of 1:3 was injected on postnatal day 1.

Injection at postnatal days 12–14. For acute expression of Kir2.1 or mNaChBac, mice previously injected with AAV2/1-EF1 α -DIO-hChR2(H134R)-EYFP between postnatal days 0 and 2 were injected with AAV2/9-hSynapsin-Flpo between postnatal days 12 and 14. Mice were anaesthetized with 2.5% isoflurane in oxygen at a flow rate of 1 l min⁻¹ and the body temperature was maintained by a feedback-based DC temperature control system at 37 °C. Buprenorphine (1 μ g) was administered subcutaneously along with 0.1 ml of Lactated Ringer's Injection. Lubricant ophthalmic ointment (Artificial Tears Ointment, Rugby Laboratories) was applied to the corneas to prevent drying. The scalp fur was shaved and the skin was cleaned with 70% alcohol and iodine. A small incision (0.5 cm) was made on the skin medial to the visual cortex. The skull at the injection site (2.5 mm lateral to the midline and 1 mm rostral to the lambda suture; the same site that was previously electroporated *in utero* and virally injected between postnatal days 0 and 2) was thinned with a 0.3-mm diameter round bur (Busch Bur, Gesswein) on a high-speed rotary micro-motor (Foredom) such that the injection glass micropipette (tip size 50- μ m outer diameter, 25- μ m inner diameter) could penetrate the skull. A total of 150 nl of virus solution was injected 450 μ m below the skull at a rate of 20 nl min⁻¹ using an UltraMicroPump III and a Micro4 controller (World Precision Instruments). After the injection, the micropipette was kept in the parenchyma for 5–10 min before being slowly withdrawn. The skin was sutured. Mice were returned to their home cage to recover from anaesthesia on a 37 °C Deltaphase Isothermal Pad.

Immunocytochemistry. Mice were anaesthetized by an intraperitoneal injection of a ketamine and xylazine mix (100 mg kg⁻¹ and 10 mg kg⁻¹, respectively), and were transcardially perfused with phosphate buffered saline (PBS, pH 7.4) followed by 4% paraformaldehyde in PBS (pH 7.4). Brains were removed, further fixed overnight in 4% paraformaldehyde, cryoprotected with 30% sucrose in PBS and frozen in optimum cutting-temperature medium until sectioning. A HM 450 Sliding Microtome (Thermo Scientific) was used to section the brains to obtain 30–50- μ m coronal slices. Slices were blocked with 1% bovine serum albumin, 2% normal goat serum and 0.3% TritonX-100 in PBS at room temperature for 1 h and incubated with primary antibodies in working buffer (0.1% bovine serum albumin, 0.2% normal goat serum, 0.3% TritonX-100 in PBS) at 4 °C overnight. The following primary antibodies were used: rabbit anti-RFP (1:200, Abcam), rat anti-RFP (1:300, Chromotek), chicken anti-GFP (1:500, Aves Labs), rabbit anti-GFP (1:2000, Life Technologies) and mouse anti-NeuN (1:200, Millipore). The slices were washed four times with working buffer for 10 min each, incubated with secondary antibodies conjugated with Alexa Fluor 488, 594 or 647 (1:500 or 1:1,000, Life Technologies) in working buffer for 1 h at room temperature, and then washed four times with working buffer for 10 min each. NeuroTrace 435/455 blue fluorescent Nissl stain (1:200, Life Technologies) was used to label neurons after antibody staining. Slices were mounted in Vectashield Mounting Medium containing 4',6-diamidino-2-phenylindole (DAPI) (Vector Laboratories) or ProLong Gold antifade reagent (Life Technologies). Images were acquired on an Olympus FV1000 Confocal, a Zeiss

Axio Imager A1 or an Olympus MVX10 Macroview, and processed using National Institutes of Health ImageJ. To estimate the fraction of layer 2/3 pyramidal cells that were transfected by *in utero* electroporation (Fig. 3a), transfected neurons (tdTomato+) and total neurons (NeuN+) in layer 2/3 were visually quantified. Assuming that 13.2% of layer 2/3 neurons are inhibitory interneurons (Extended Data Fig. 3), we estimated that $9 \pm 1\%$ (mean \pm s.e.m., $n = 12$ sections from six mice) of layer 2/3 pyramidal cells were transfected.

In vitro physiology. Mice between postnatal days 14 and 23 were anaesthetized by an intraperitoneal injection of a ketamine and xylazine mix (100 mg kg^{-1} and 10 mg kg^{-1} , respectively), and transcardially perfused with cold ($0-4^\circ\text{C}$) slice cutting solution containing 80 mM NaCl , 2.5 mM KCl , $1.3 \text{ mM NaH}_2\text{PO}_4$, 26 mM NaHCO_3 , 4 mM MgCl_2 , 0.5 mM CaCl_2 , 20 mM D-glucose , 75 mM sucrose and $0.5 \text{ mM sodium ascorbate}$ (315 mosmol , $\text{pH } 7.4$, saturated with $95\% \text{ O}_2/5\% \text{ CO}_2$). Brains were removed and sectioned in the cutting solution with a Super Microslicer Zero1 (D.S.K.) to obtain $300\text{-}\mu\text{m}$ coronal slices. Slices were incubated in a custom-made interface holding chamber saturated with $95\% \text{ O}_2/5\% \text{ CO}_2$ at 34°C for 30 min and then at room temperature for 20 min to 8 h until they were transferred to the recording chamber.

Recordings were performed on submerged slices in artificial cerebrospinal fluid (ACSF) containing 119 mM NaCl , 2.5 mM KCl , $1.3 \text{ mM NaH}_2\text{PO}_4$, 26 mM NaHCO_3 , 1.3 mM MgCl_2 , 2.5 mM CaCl_2 , 20 mM D-glucose and $0.5 \text{ mM sodium ascorbate}$ (300 mosmol , $\text{pH } 7.4$, saturated with $95\% \text{ O}_2/5\% \text{ CO}_2$, perfused at 3 ml min^{-1}) at $31-32^\circ\text{C}$. For whole-cell recordings, we used a K^+ -based pipette solution containing 142 mM K^+ -gluconate, 10 mM HEPES , 1 mM EGTA , 2.5 mM MgCl_2 , 4 mM ATP-Mg , 0.3 mM GTP-Na , 10 mM Na_2 -phosphocreatine (295 mosmol , $\text{pH } 7.35$) or a Cs^+ -based pipette solution containing 115 mM Cs^+ -methanesulphonate, 10 mM HEPES , 1 mM EGTA , 1.5 mM MgCl_2 , 4 mM ATP-Mg , 0.3 mM GTP-Na , 10 mM Na_2 -phosphocreatine, $2 \text{ mM QX } 314\text{-Cl}$, $10 \text{ mM BAFTA-tetracesium}$ (295 mosmol , $\text{pH } 7.35$). Membrane potentials were not corrected for liquid junction potential (experimentally measured as 11.4 mV for the K^+ -based pipette solution and 8.4 mV for the Cs^+ -based pipette solution).

Neurons were visualized with video-assisted infrared differential interference contrast imaging and fluorescent neurons were identified by epifluorescence imaging under a water immersion objective ($\times 40$, 0.8 numerical aperture) on an upright Olympus BX51WI microscope with an infrared CCD camera (VX44, Till Photonics). For Fos-EGFP experiments, in a given field-of-view those pyramidal cells with the strongest EGFP fluorescence were visually identified as the EGFP+ neurons. The EGFP- neurons were those pyramidal cells whose fluorescence was equal to the background fluorescence level of the slices.

Data were low-pass filtered at 4 kHz and acquired at 10 kHz with an Axon Multiclamp 700A or 700B amplifier and an Axon Digidata 1440A Data Acquisition System under the control of Clampex 10.2 (Molecular Devices). Data were analysed offline using AxoGraph X (AxoGraph Scientific).

For the photostimulation of Chr2-expressing neurons, blue light was emitted from a collimated light-emitting diode (470 nm) driven by a T-Cube LED Driver (Thorlabs) under the control of an Axon Digidata 1440A Data Acquisition System and Clampex 10.2. Light was delivered through the reflected light fluorescence illuminator port and the $\times 40$ objective.

Synaptic currents were recorded in the whole-cell voltage clamp mode with the Cs^+ -based patch pipette solution. Only recordings with series resistance below $20 \text{ M}\Omega$ were included. EPSCs and IPSCs were recorded at the reversal potential for IPSCs (-60 mV) and EPSCs ($+10 \text{ mV}$), respectively. For light pulse stimulation, pulse duration ($0.5-5 \text{ ms}$) and intensity ($1.1-5.5 \text{ mW mm}^{-2}$) were adjusted for each recording to evoke small (to minimize voltage-clamp errors; see the figures for the ranges) but reliable monosynaptic EPSCs or IPSCs. Disynaptic IPSCs were evoked using the same light pulses that were used for evoking the corresponding monosynaptic EPSCs. Light pulses were delivered at 30-s interstimulus intervals.

To quantify the inter-cell variability of EPSCs (Fig. 1d, f), we used the average relative deviation defined as $\frac{1}{N \times \text{EPSC}_{\text{mean}}} \sum_{i=1}^N |\text{EPSC}_i - \text{EPSC}_{\text{mean}}|$, where N is the number of pyramidal cells in one given experiment, EPSC_i is the amplitude of the EPSC recorded in the i^{th} pyramidal cell within that experiment and $\text{EPSC}_{\text{mean}}$ is the mean amplitude of EPSCs recorded across pyramidal cells in the same experiment. The average relative deviation of IPSCs or E/I ratios was obtained in the same way for each experiment (Fig. 1d, f).

To record unitary connections between inhibitory neurons and pyramidal cells, Pvalb and Sst cells were identified by the Cre-dependent expression of Chr2-tdTomato or hChr2(H134R)-EYFP in *Pvalb-ires-Cre* and *Sst-ires-Cre* mice, respectively. Pyramidal cells were first recorded in whole-cell voltage clamp mode ($+10 \text{ mV}$) with the Cs^+ -based patch pipette solution, and a nearby Pvalb or Sst cell was subsequently recorded in the whole-cell current clamp mode with the K^+ -based patch pipette solution. Action potentials were elicited in Pvalb or Sst cells by a 2-ms depolarizing current step ($1-2 \text{ nA}$) with a 15-s interstimulus intervals.

Unitary IPSC (uIPSC) amplitudes were measured from the average of 10–50 sweeps. We considered a Pvalb or Sst cell to be connected with a pyramidal cell when the average uIPSC amplitude was at least three times the baseline standard deviation. The average relative deviation of uIPSC amplitudes (Fig. 5 and Extended

Data Fig. 9) was calculated as $\frac{1}{N \times \text{uIPSC}_{\text{mean}}} \sum_{i=1}^N |\text{uIPSC}_i - \text{uIPSC}_{\text{mean}}|$ where N is the number of pyramidal cells in one given experiment, uIPSC_i is the amplitude of the IPSC recorded in the i^{th} pyramidal cell within that experiment and $\text{uIPSC}_{\text{mean}}$ is the mean amplitude of uIPSCs recorded across pyramidal cells in the same experiment.

Neuronal intrinsic excitability was examined with the K^+ -based pipette solution in the presence of the AMPA receptor antagonist NBQX ($10 \mu\text{M}$), the NMDA receptor antagonist (RS)-CPP ($10 \mu\text{M}$) and the GABA_A (γ -aminobutyric acid) receptor antagonist SR 95531 ($10 \mu\text{M}$). The resting membrane potential was recorded in the whole-cell current clamp mode within the first minute after break-in. The input resistance was measured after balancing the bridge by injecting a 500-ms-long hyperpolarizing current pulse ($10-100 \text{ pA}$) to generate a small membrane potential hyperpolarization ($2-10 \text{ mV}$) from the resting membrane potential. Depolarizing currents were increased in 5- or 10-pA steps to identify rheobase currents.

Ba^{2+} -sensitive currents were measured with the K^+ -based pipette solution in the presence of NBQX ($10 \mu\text{M}$), (RS)-CPP ($10 \mu\text{M}$), SR 95531 ($10 \mu\text{M}$) and Na^+ channel blocker TTX ($1 \mu\text{M}$). Only recordings with series resistance below $20 \text{ M}\Omega$ were included. Neurons were clamped at -25 mV and the membrane potential was ramped to -125 mV at a rate of 20 mV s^{-1} . The membrane currents recorded in the presence of BaCl_2 ($50 \mu\text{M}$) were subtracted from those recorded in the absence of BaCl_2 to obtain the Ba^{2+} -sensitive currents, which were then divided by the whole-cell membrane capacitances to calculate the current densities.

In vivo physiology. Mice between postnatal days 17 and 23 were anaesthetized by an intraperitoneal injection of chlorprothixene (5 mg kg^{-1}) followed by urethane (1.2 g kg^{-1}). Oxygen was given at a flow rate of 1 l min^{-1} during the experiments and isoflurane ($<0.5\%$) was supplemented if necessary. The body temperature was maintained by a feedback-based DC temperature control system at 37°C . Dexamethasone sodium phosphate (2 mg kg^{-1}) and Lactated Ringer's Injection (3 ml kg^{-1} every 2 h) were administered subcutaneously. Whiskers and eyelashes were trimmed, and a thin layer of silicone oil (kinematic viscosity $30,000$ centistokes ($1 \text{ cSt} = 10^{-6} \text{ m}^2 \text{ s}^{-1}$), Sigma-Aldrich) was applied to the corneas to prevent drying. The scalp and periosteum were removed. Vetbond tissue adhesive (3M) was applied to stabilize all sutures. A custom-made recording chamber with a 3-mm diameter hole in the centre was attached to the skull over V1 with Vetbond tissue adhesive and dental cement (Ortho-Jet BCA, Lang Dental). The recording chamber was then secured on a custom-made holder. A craniotomy ($1.5-2 \text{ mm}$ diameter, centred at 2.5 mm lateral to midline and 1 mm rostral to lambda suture) was performed with a 0.3-mm diameter round bur on a high-speed rotary micromotor. The dura was left intact and the craniotomy was covered by a thin layer of 1.5% type III-A agarose in HEPES-ACSF containing 142 mM NaCl , 5 mM KCl , 10 HEPES-Na , 1.3 mM MgCl_2 , 3.1 mM CaCl_2 and 10 mM D-glucose (310 mosmol , $\text{pH } 7.4$). HEPES-ACSF was added to the recording chamber.

Targeted loose-patch recordings were performed under the guidance of a two-photon laser scanning microscope. Two-photon imaging was performed with a water immersion objective ($\times 40$, 0.8 numerical aperture, Olympus) on a Moveable Objective Microscope (Sutter Instruments) coupled with a Ti:Sapphire laser (Chameleon Ultra II, Coherent) under the control of ScanImage 3.6 (Janelia Farm Research Campus, HHMI)⁴⁷. Laser wavelength was tuned to 950 nm (laser power after the objective: $25-50 \text{ mW}$) for two-photon excitation of tdTomato and Alexa Fluor 488.

An Axon Multiclamp 700B amplifier was used for extracellular recording of spikes. A patch pipette containing HEPES-ACSF and $10-20 \mu\text{M}$ Alexa Fluor 488 hydrazide (Life Technologies) was advanced along its axis towards neurons located between 150 and $250 \mu\text{m}$ below the dura with minimal lateral movements. A small positive pressure was applied to the patch pipette to avoid clogging of the tip and to inject a small amount of fluorescent dye to stain the extracellular space. Non-fluorescent neurons were visualized as negative images⁴⁸. The pipette resistance was constantly monitored in voltage-clamp mode. The concurrence of the pipette tip contacting the neuron and an increase in pipette resistance indicated successful targeting, which was further confirmed post hoc (see below). Upon the release of positive pressure, a small negative pressure was applied to form a loose seal ($10-30 \text{ M}\Omega$). The amplifier was then switched to the current-clamp mode with zero current injection to record voltage. Data were low-pass filtered at 10 kHz and acquired at 32 kHz with a NI-DAQ board (NI PCIe-6259, National Instruments) under the control of a custom-written program running in Matlab (Mathworks). Within a local region ($<50 \mu\text{m}$), neighbouring tdTomato⁺ and tdTomato⁻ neurons were sequentially targeted for recording, but the order of recordings from tdTomato⁺ and tdTomato⁻ was alternated. The correct targeting of tdTomato⁺ neurons was confirmed at the end of the recording either by the filling of the neuron with the

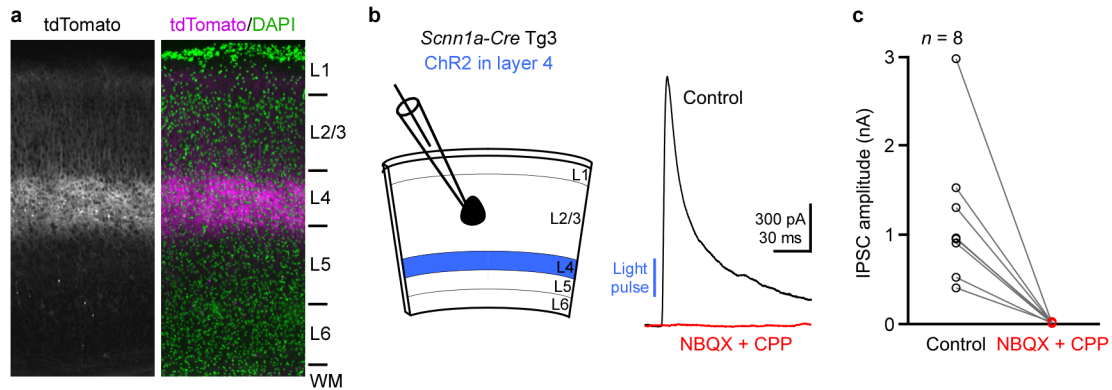
fluorescent dye contained in the pipette via break-in or by the presence of neuronal fluorescence in the recording pipette due to the negative pressure.

Visual stimuli were generated in Matlab with Psychophysics Toolbox⁴⁹ and displayed on a gamma-corrected liquid-crystal display monitor (30 cm × 47.5 cm, 60 Hz refresh rate, mean luminance 50 cd m⁻²). The monitor was placed 25 cm away from the contralateral eye, covering 62° (vertical) × 87° (horizontal) of the visual space. The monitor was approximately centred at the retinotopic location corresponding to the V1 recording site by monitoring single-unit or multi-unit activity in response to a moving bar on the screen. During recordings, full-field sinusoidal drifting gratings (temporal frequency 2 Hz, spatial frequency 0.04 cycles per degree, 100% contrast) were presented randomly at 12 different directions from 0° to 330° for 1.5 s, preceded and followed by the presentation of a grey screen for 2 s and 1.5 s, respectively. The complete set of stimuli was repeated 8–16 times.

We analysed data offline using a custom-written program in Matlab. Voltage signals were high-pass filtered (125 Hz). Spikes were first detected as events exceeding five times the standard deviation of the noise, and then visually verified. Spontaneous spike rate was calculated as the average spike rate during the 2-s time window before the presentation of a visual stimulus. Evoked spike rate was calculated as the average spike rate during the 1.5-s time window of visual stimulation. Overall spike rate was calculated as the average spike rate during the entire recording period.

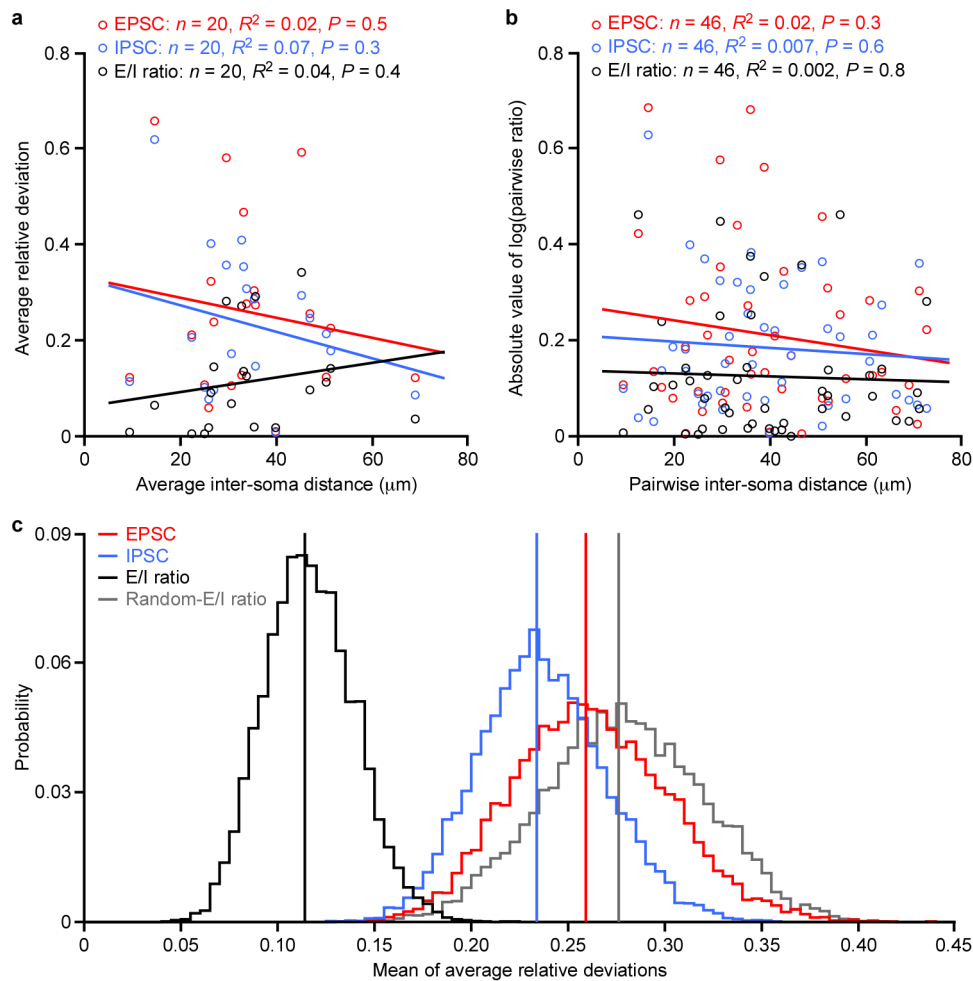
Statistics. All reported sample numbers (*n*) represent biological replicates. Sample sizes were estimated to have 70–80% power to detect expected effect size using StatMate 2 (GraphPad Software). Statistical analyses used Prism 5 (GraphPad Software) and Matlab. Linear regression with an *F*-test (two-sided) was used for Fig. 1e and Extended Data Fig. 2a, b. Bootstrapped distributions (Extended Data Fig. 2c) were used to determine the statistical significance for Fig. 1f. A Wilcoxon matched-pairs signed rank test (two-sided) was used for Figs 2, 3h–j, 4, 5b and Extended Data Figs 1–5. A Mann–Whitney *U*-test (two-sided) was used for Fig. 3d–f, uIPSC amplitudes in Figs 5f, g and Extended Data Figs 4, 6, 9c, d. Fisher's exact test (two-sided) was used for connectivity rates in Fig. 5f and Extended Data Fig. 9b.

31. Madisen, L. *et al.* A robust and high-throughput Cre reporting and characterization system for the whole mouse brain. *Nature Neurosci.* **13**, 133–140 (2010).
32. Barth, A. L., Gerkin, R. C. & Dean, K. L. Alteration of neuronal firing properties after *in vivo* experience in a FosGFP transgenic mouse. *J. Neurosci.* **24**, 6466–6475 (2004).
33. Taniguchi, H. *et al.* A resource of Cre driver lines for genetic targeting of GABAergic neurons in cerebral cortex. *Neuron* **71**, 995–1013 (2011).
34. Hippenmeyer, S. *et al.* A developmental switch in the response of DRG neurons to ETS transcription factor signaling. *PLoS Biol.* **3**, e159 (2005).
35. Yang, J., Jan, Y. N. & Jan, L. Y. Control of rectification and permeation by residues in two distinct domains in an inward rectifier K⁺ channel. *Neuron* **14**, 1047–1054 (1995).
36. Tong, Y. *et al.* Tyrosine decaging leads to substantial membrane trafficking during modulation of an inward rectifier potassium channel. *J. Gen. Physiol.* **117**, 103–118 (2001).
37. Tinker, A., Jan, Y. N. & Jan, L. Y. Regions responsible for the assembly of inwardly rectifying potassium channels. *Cell* **87**, 857–868 (1996).
38. Ren, D. *et al.* A prokaryotic voltage-gated sodium channel. *Science* **294**, 2372–2375 (2001).
39. Yue, L., Navarro, B., Ren, D., Ramos, A. & Clapham, D. E. The cation selectivity filter of the bacterial sodium channel, NaChBac. *J. Gen. Physiol.* **120**, 845–853 (2002).
40. Turan, S., Kuehle, J., Schambach, A., Baum, C. & Bode, J. Multiplexing RMCE: versatile extensions of the Flp-recombinase-mediated cassette-exchange technology. *J. Mol. Biol.* **402**, 52–69 (2010).
41. Kranz, A. *et al.* An improved Flp deleter mouse in C57Bl/6 based on FlpO recombinase. *Genesis* **48**, 512–520 (2010).
42. Matsuda, T. & Cepko, C. L. Electroporation and RNA interference in the rodent retina *in vivo* and *in vitro*. *Proc. Natl Acad. Sci. USA* **101**, 16–22 (2004).
43. Manent, J. B., Wang, Y., Chang, Y., Paramasivam, M. & LoTurco, J. J. Dcx reexpression reduces subcortical band heterotopia and seizure threshold in an animal model of neuronal migration disorder. *Nature Med.* **15**, 84–90 (2009).
44. Matsuda, T. & Cepko, C. L. Controlled expression of transgenes introduced by *in vivo* electroporation. *Proc. Natl Acad. Sci. USA* **104**, 1027–1032 (2007).
45. Atasoy, D., Aponte, Y., Su, H. H. & Sternson, S. M. A FLEX switch targets channelrhodopsin-2 to multiple cell types for imaging and long-range circuit mapping. *J. Neurosci.* **28**, 7025–7030 (2008).
46. Sohal, V. S., Zhang, F., Yizhar, O. & Deisseroth, K. Parvalbumin neurons and gamma rhythms enhance cortical circuit performance. *Nature* **459**, 698–702 (2009).
47. Pologruto, T. A., Sabatini, B. L. & Svoboda, K. ScanImage: flexible software for operating laser scanning microscopes. *Biomed. Eng. Online* **2**, 13 (2003).
48. Kitamura, K., Judkewitz, B., Kano, M., Denk, W. & Hausser, M. Targeted patch-clamp recordings and single-cell electroporation of unlabeled neurons *in vivo*. *Nature Methods* **5**, 61–67 (2008).
49. Brainard, D. H. The Psychophysics Toolbox. *Spat. Vis.* **10**, 433–436 (1997).
50. Hibino, H. *et al.* Inwardly rectifying potassium channels: their structure, function, and physiological roles. *Physiol. Rev.* **90**, 291–366 (2010).



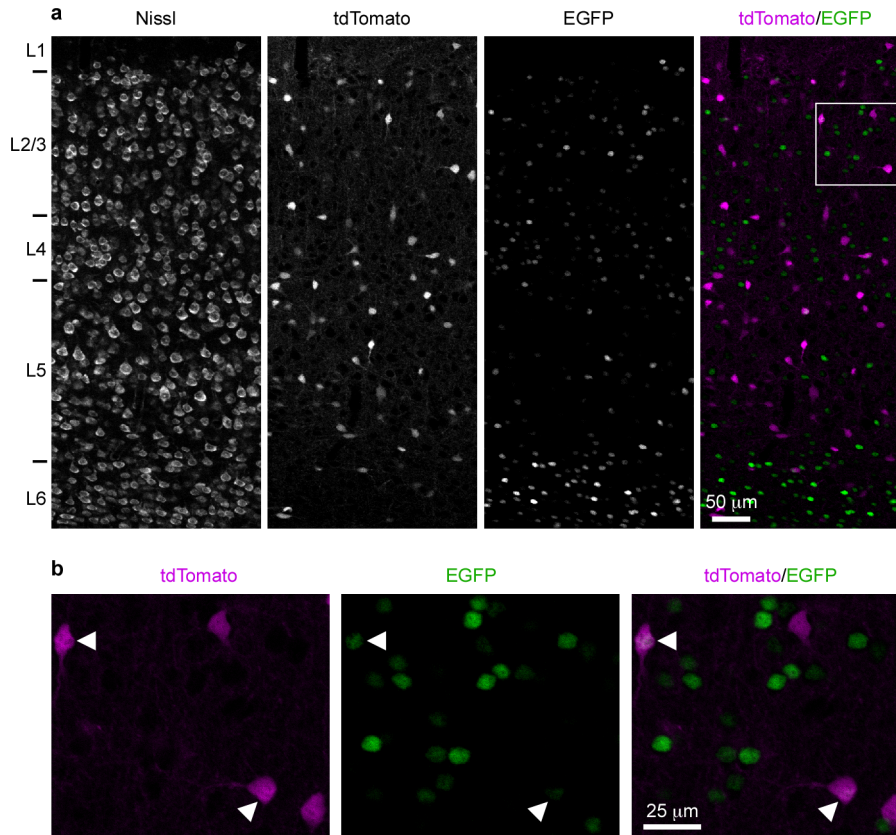
Extended Data Figure 1 | Cre recombinase-expressing cells in the cortex of *Scnn1a-Cre-Tg3* mice are layer 4 excitatory neurons. AAV-CAGGS-Flex-ChR2-tdTomato, expressing ChR2-tdTomato fusion protein in a Cre-dependent manner, was injected into *Scnn1a-Cre-Tg3* mice. **a**, Representative fluorescent images of a coronal section of V1 showing that the ChR2-tdTomato-expressing cells located primarily in layer 4 ($n = 11$ mice). Cortical layers are indicated on the right based on the DAPI staining pattern. L, layer; WM, white matter. **b**, Left, schematic of experiments. Right, a layer 2/3

pyramidal cell was voltage clamped at the reversal potential for excitation (+10 mV). Photoactivation of ChR2-expressing neurons in layer 4 elicited an IPSC (black trace), which was abolished by the glutamatergic receptor antagonists NBQX and CPP (red trace), indicating its disynaptic nature. **c**, Summary data: NBQX and CPP reduced IPSC amplitudes by $98.0 \pm 0.6\%$ (mean \pm s.e.m., $n = 8$, $P = 0.008$) indicating that ChR2 was exclusively expressed in excitatory neurons.



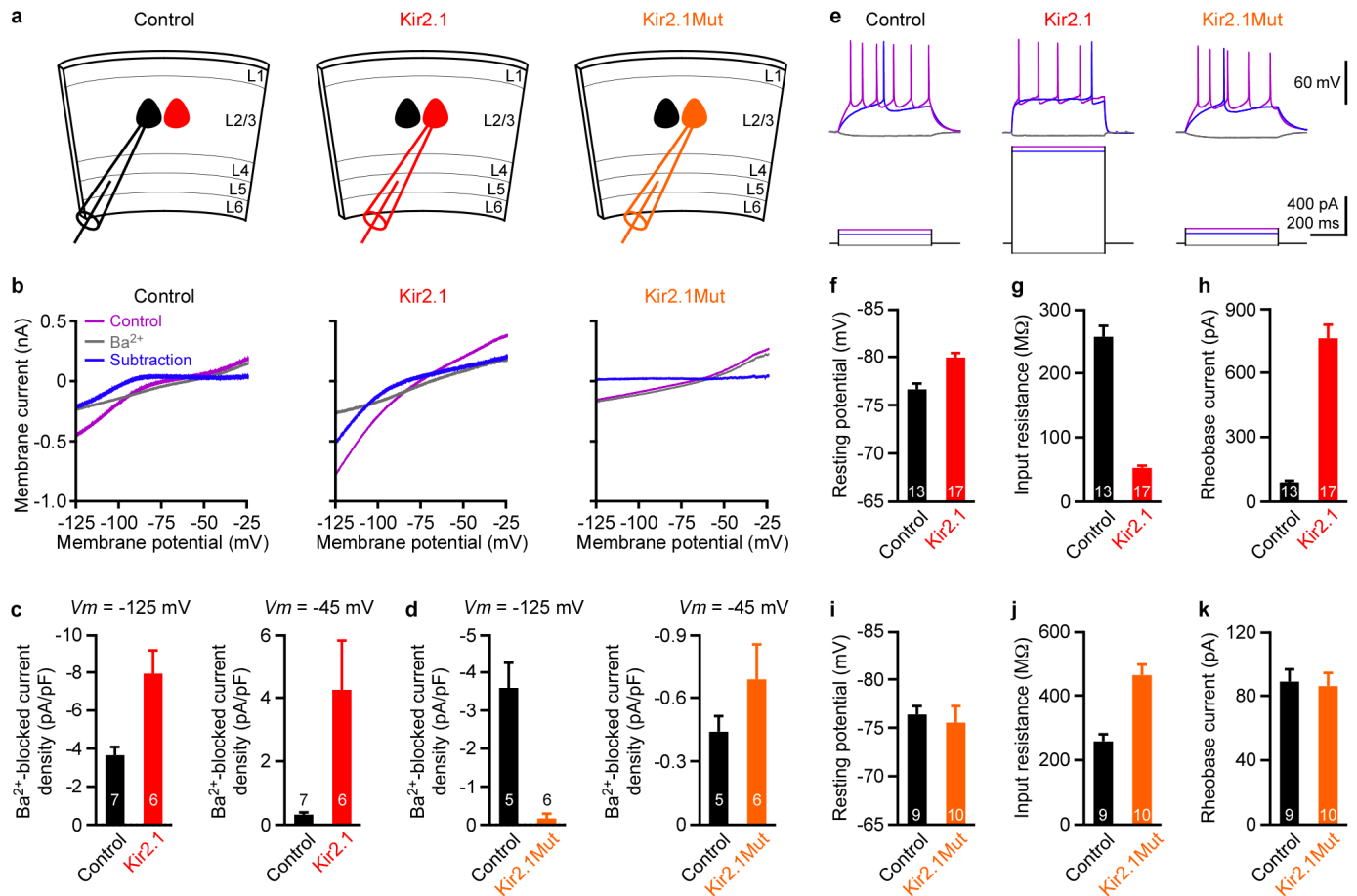
Extended Data Figure 2 | Characterization of the inter-cell variability of EPSCs, IPSCs and E/I ratios. **a, b,** The inter-cell variability of EPSCs, IPSCs and E/I ratios among neighbouring pyramidal cells does not correlate with their inter-soma distances. **a,** The average relative deviations of EPSCs, IPSCs and E/I ratios from each experiment in Fig. 1f are plotted against the average inter-soma distance from the same experiment. The average inter-soma distance is the mean of the distances between each pair of pyramidal cells. For the experiments in which only two pyramidal cells were recorded, the inter-soma distance between the two pyramidal cells was used. Lines, linear regression fits. **b,** The absolute value of the logarithm of the ratio of EPSCs (or IPSCs or E/I ratios) simultaneously recorded in two pyramidal cells was plotted against the inter-somatic distance between the two cells. **c,** The distribution of E/I ratios across pyramidal cells varies less than if EPSCs and IPSCs were randomly paired between cells and less than the distributions of EPSC and IPSC amplitudes. To determine whether the precise E/I ratio recorded within each pyramidal cell minimizes the average relative deviation, we computed the E/I ratios from randomly but uniquely paired EPSCs and IPSCs within each of the 20 experiments from Fig. 1f. By randomizing within each experiment, we ensured that the average relative deviation was only modified owing to the pairing of EPSCs to IPSCs. Note that, for an experiment with N pyramidal cells, there were $N!$ possible randomized pairings of EPSCs and IPSCs, and hence $N!$ possible E/I ratio average relative deviations (referred to as random-E/I ratio

average relative deviations). The distribution of the means of the random-E/I ratio average relative deviations (grey histogram) was constructed from the means of 10,000 samples. Each sample consisted of 20 random-E/I ratio average relative deviations, each of which was randomly chosen from the $N!$ possible random-E/I ratio average relative deviations of each experiment. The grey vertical line represents the mean of the distribution. The distribution of the means of the E/I ratio average relative deviations (black histogram) was generated by bootstrapping (that is, resampling 10,000 times with replacement). Each resample consisted of 20 randomly chosen E/I ratio average relative deviations from the 20 experiments in Fig. 1f, and an E/I ratio average relative deviation was allowed to be repeated within one resample (that is, sampling with replacement). The black vertical line represents the mean of the experimentally obtained E/I ratio average relative deviations. The E/I ratio average relative deviations are smaller than the random-E/I ratio average relative deviations ($P < 0.0001$). The distributions of the means of the EPSC average relative deviations (red histogram) and the means of the IPSC average relative deviations (blue histogram) were generated by similar bootstrapping to the E/I ratio average relative deviations. The red and blue vertical lines represent the means of the experimentally obtained EPSC average relative deviations and IPSC average relative deviations, respectively. The E/I ratio average relative deviations are smaller than the EPSC average relative deviations ($P < 0.0001$) and the IPSC average relative deviations ($P < 0.0001$).



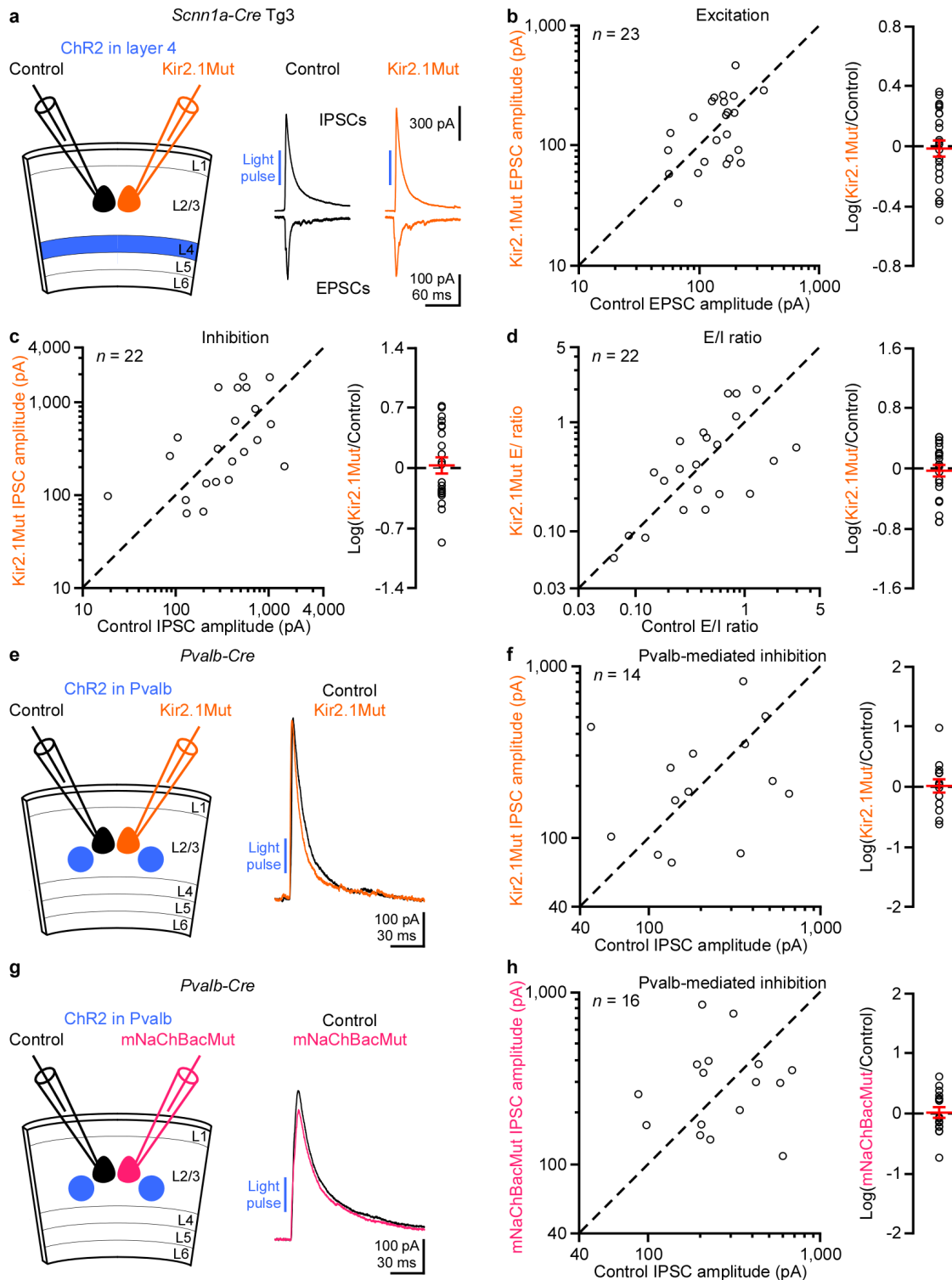
Extended Data Figure 3 | Most layer 2/3 Fos-EGFP+ neurons in V1 are pyramidal cells. *Fos-EGFP* mice were crossed with *Gad2-ires-Cre* and *Rosa-CAG-LSL-tdTomato-WPRE* mice to generate *Fos-EGFP, Gad2-ires-Cre, Rosa-CAG-LSL-tdTomato-WPRE* mice. **a**, Representative fluorescent images showed a coronal section of V1. All neurons were visualized by NeuroTrace 435/455 blue fluorescent Nissl stain and GABAergic interneurons were labelled by tdTomato. EGFP was stained with an antibody against GFP and visualized with a secondary antibody conjugated with Alexa Fluor 647. Cortical layers are

indicated on the left based on the Nissl staining pattern. **b**, Enlarged view of the boxed region in **a**. In layer 2/3 of V1, only $5.3 \pm 0.9\%$ (mean \pm s.e.m., $n = 10$ sections from two mice) of EGFP+ neurons were GABAergic interneurons (two examples are indicated by arrowheads). GABAergic interneurons constitute $13.2 \pm 0.6\%$ (mean \pm s.e.m., $n = 14$ sections from three mice including one *Gad2-ires-Cre, Rosa-CAG-LSL-tdTomato-WPRE* mouse) of all layer 2/3 neurons.



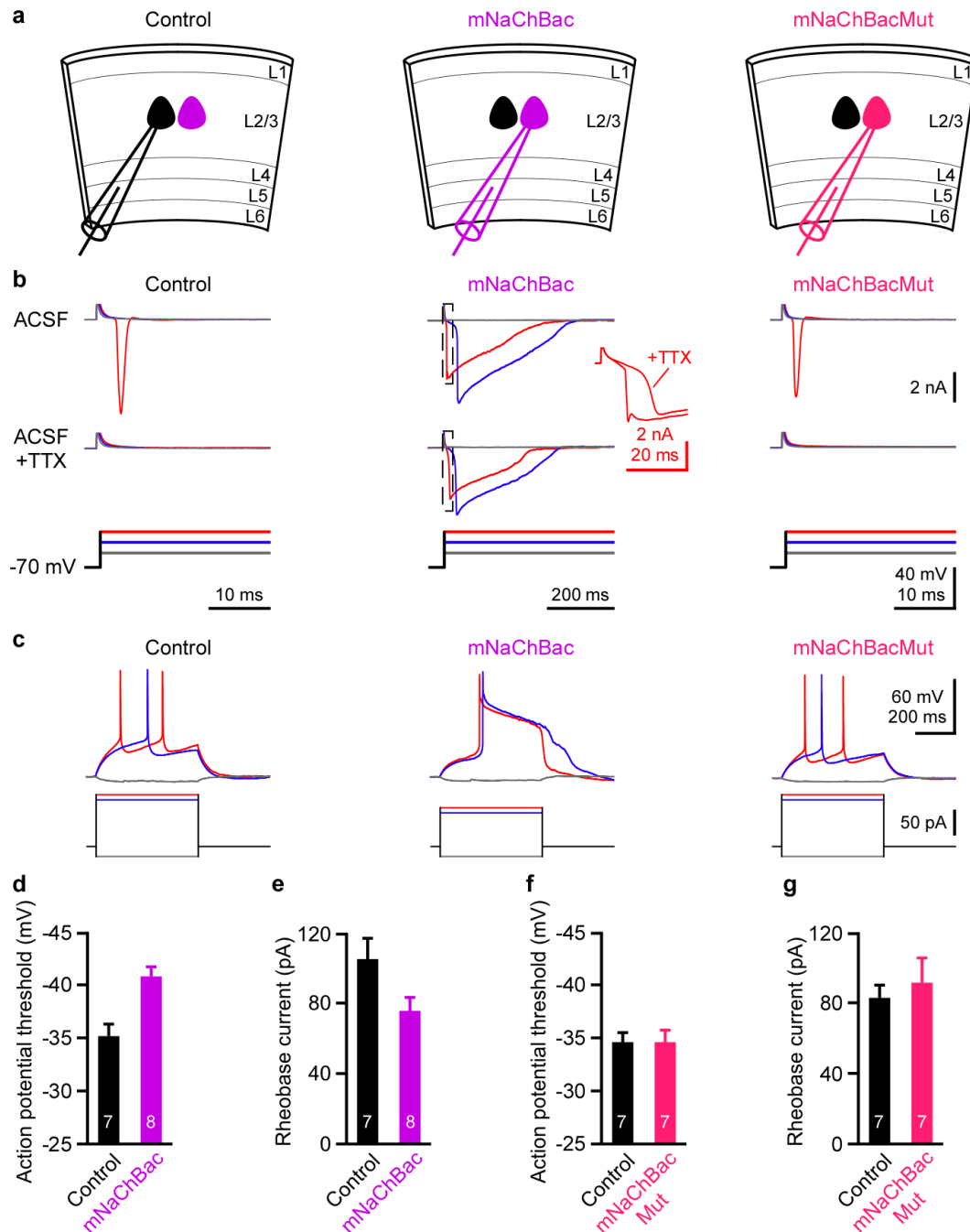
Extended Data Figure 4 | Overexpression of Kir2.1 increases a Ba²⁺-sensitive K⁺ current and decreases neuronal excitability. **a**, Schematics of experiments. Kir2.1 or a non-conducting mutant Kir2.1 (Kir2.1Mut) was overexpressed in a subset of layer 2/3 pyramidal cells by *in utero* electroporation. **b**, Membrane currents in response to a 5 s membrane potential ramp from -25 to -125 mV from an untransfected control pyramidal cell, a pyramidal cell overexpressing Kir2.1 and a pyramidal cell overexpressing Kir2.1Mut. The purple traces were recorded in control condition and the grey traces were recorded in the presence of 50 μM BaCl₂, a concentration that primarily blocks the K⁺ channels of the Kir2 subfamily⁵⁰. The blue traces were obtained by subtracting the grey traces from the purple traces, representing the Ba²⁺-blocked K⁺ currents. **c**, The exogenously overexpressed Kir2.1 increased not only the Ba²⁺-blocked inward current density at -125 mV ($P = 0.01$), but also the outward current density at -45 mV ($P = 0.001$) owing

to its reduced inward rectification (see Methods). **d**, Kir2.1Mut can bind to the endogenous Kir2.1 to form non-conducting channels⁵⁰, acting as a dominant negative to decrease the inward current density at -125 mV ($P = 0.004$) but without affecting the outward current density at -45 mV ($P = 0.2$). **e**, Membrane potentials (upper panels) in response to current injections (lower panels) from an untransfected control pyramidal cell, a pyramidal cell overexpressing Kir2.1 and a pyramidal cell overexpressing Kir2.1Mut. **f-h**, Overexpression of Kir2.1 hyperpolarized the resting membrane potential (**f**, $P = 0.0003$), decreased the resting input resistance (**g**, $P < 0.0001$) and increased the rheobase current (**h**, $P < 0.0001$). **i-k**, Overexpression of Kir2.1Mut increased the resting input resistance (**j**, $P = 0.0002$), but had no effects on the resting membrane potential (**i**, $P = 0.5$) and the rheobase current (**k**, $P = 0.9$). The numbers of recorded neurons are indicated on the bars. All data are expressed as mean ± s.e.m.



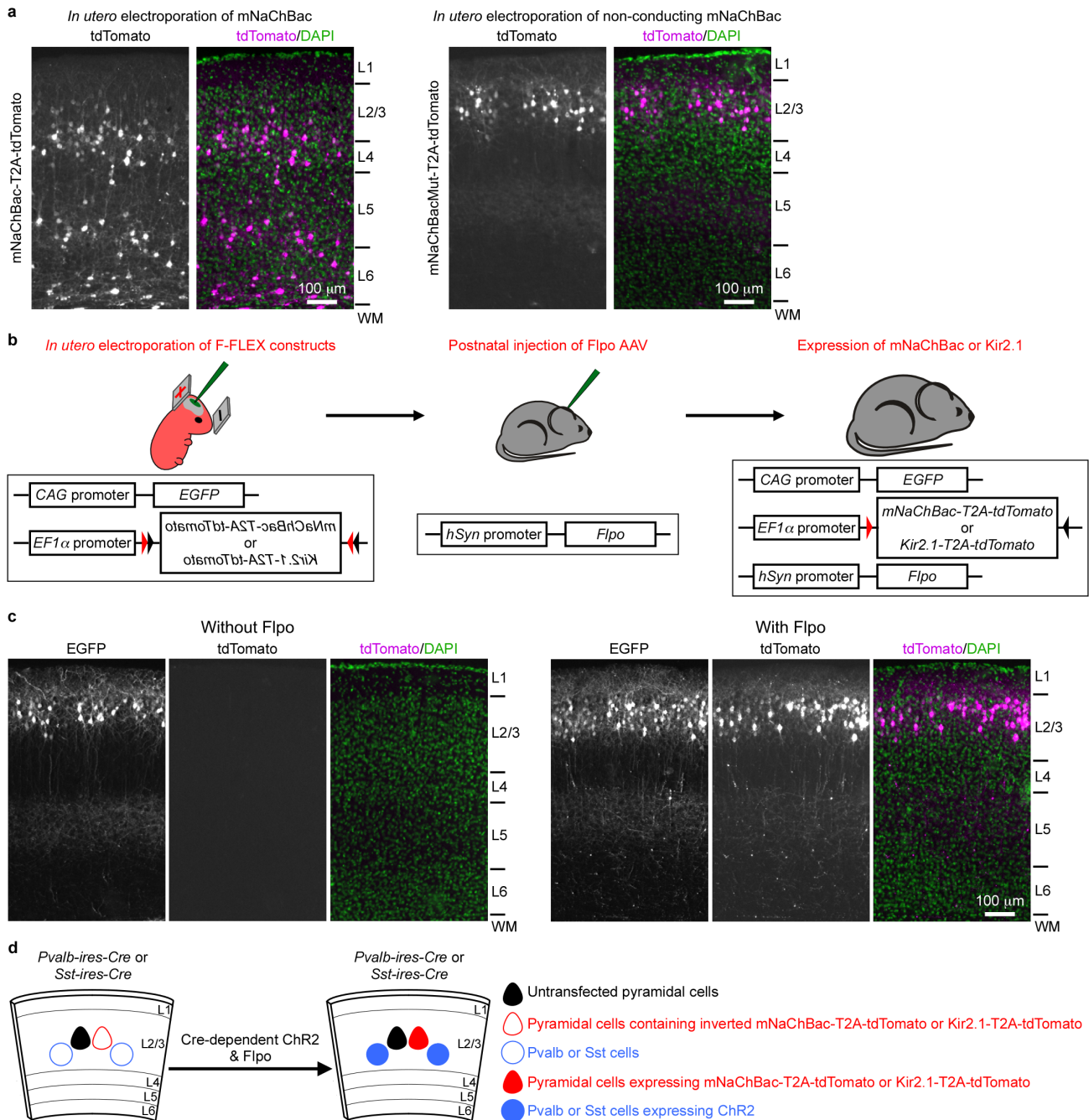
Extended Data Figure 5 | Overexpression of Kir2.1Mut or mNaChBacMut in layer 2/3 pyramidal cells does not affect inhibition. **a**, Left, schematic of experiments. *Scnn1a-Cre-Tg3* mice with ChR2 in layer 4 excitatory neurons and Kir2.1Mut in a subset of layer 2/3 pyramidal cells. Right, monosynaptic EPSCs and disynaptic IPSCs from simultaneously recorded control and Kir2.1Mut neurons in response to layer 4 photoactivation. **b–d**, Summary graphs. **b**, Left, EPSC amplitudes in Kir2.1Mut neurons plotted against those in control neurons. Right, logarithm of the ratio between EPSC amplitudes in Kir2.1Mut and control neurons. Red, mean \pm s.e.m. EPSC amplitudes are similar between Kir2.1Mut and control neurons ($n = 23$, $P = 0.7$). **c**, As in **b**, but for IPSCs. IPSC amplitudes are similar between Kir2.1Mut and control neurons ($n = 22$, $P = 0.6$). **d**, As in **b**, but for E/I ratios. E/I ratios are similar

between Kir2.1 and control neurons ($n = 22$, $P = 0.6$). **e**, Left, schematic of experiments. *Pvalb-ires-Cre* mice with ChR2 in Pvalb cells and Kir2.1Mut in a subset of layer 2/3 pyramidal cells. Right, IPSCs from simultaneously recorded control and Kir2.1Mut neurons in response to Pvalb cell photoactivation. **f**, Summary graphs. Left, IPSC amplitudes in Kir2.1Mut neurons plotted against those in control neurons. Right, logarithm of the ratio between IPSC amplitudes in Kir2.1Mut and control neurons. Red, mean \pm s.e.m. IPSC amplitudes are similar between Kir2.1Mut and control neurons ($n = 14$, $P = 0.8$). **g**, **h**, As in **e**, **f**, but for a non-conducting mutant mNaChBac (mNaChBacMut). IPSC amplitudes are similar between mNaChBacMut and control neurons ($n = 16$, $P = 0.9$).



Extended Data Figure 6 | Overexpression of mNaChBac increases neuronal excitability. **a**, Schematics of experiments. mNaChBac or a non-conducting mutant mNaChBac (mNaChBacMut) was overexpressed in a subset of layer 2/3 pyramidal cells by *in utero* electroporation. **b**, Membrane currents (upper and middle panels) in response to voltage steps (lower panels) from an untransfected control pyramidal cell, a pyramidal cell overexpressing mNaChBac and a pyramidal cell overexpressing mNaChBacMut. The endogenous voltage-gated inward Na^+ current was fast inactivating and was blocked by tetrodotoxin (TTX, $1 \mu\text{M}$), whereas the mNaChBac-mediated inward current was slow inactivating and insensitive to TTX. Inset, overlay of the two dashed boxes. Note that the fast component of the inward current representing the endogenous Na^+ current was blocked by TTX. **c**, Membrane

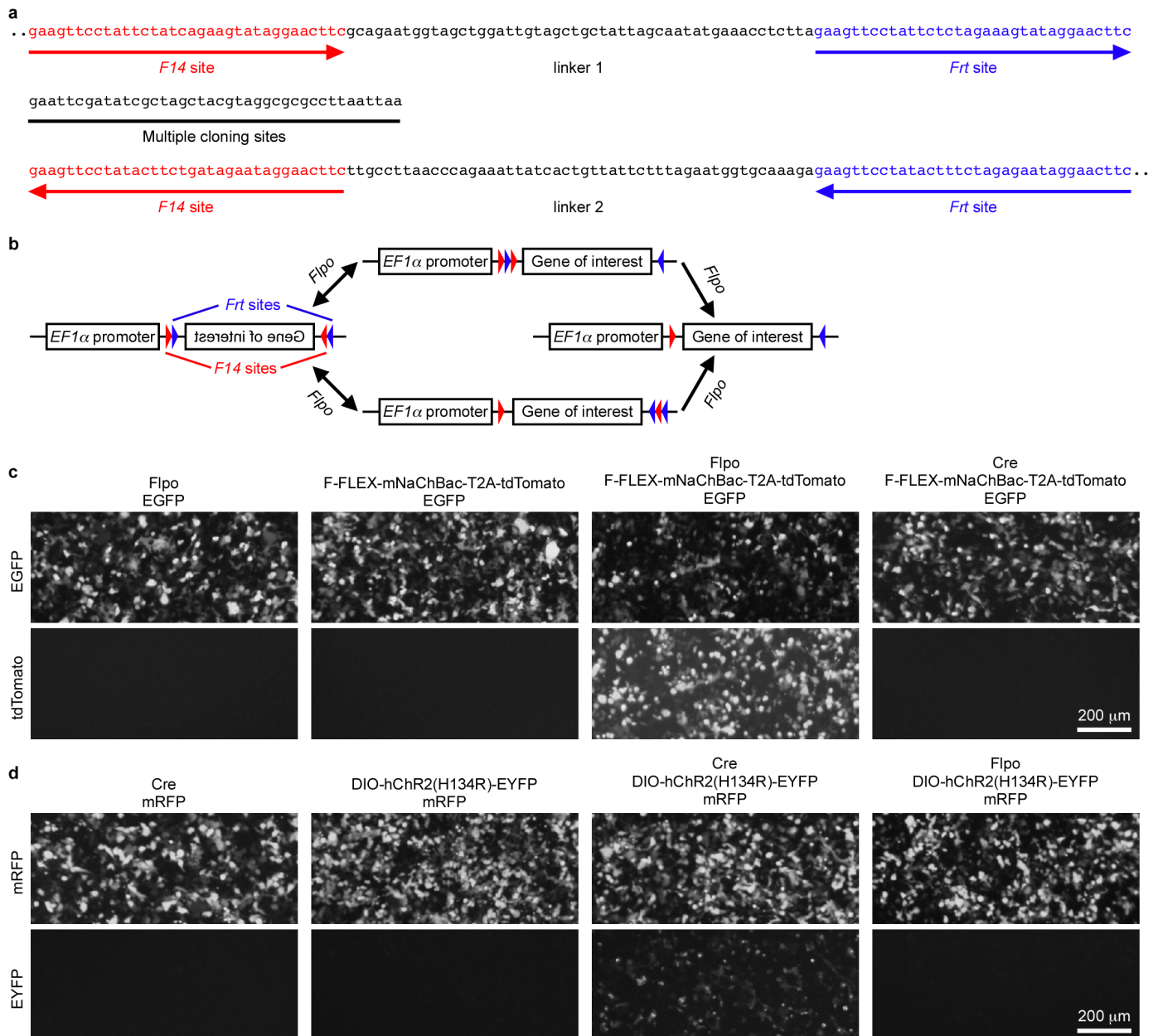
potentials (upper panels) in response to current injections (lower panels) from a control neuron, a mNaChBac neuron and a mNaChBacMut neuron. The mNaChBac neuron generated long-lasting action potentials and depolarizations, whereas the mNaChBacMut neuron generated action potentials similar to the control neuron. **d**, **e**, Overexpression of mNaChBac lowered the action potential threshold (defined as the membrane potential whose derivative reaches 2 V s^{-1}) (**d**, $P = 0.004$) and decreased the rheobase current (**e**, $P = 0.03$). **f**, **g**, Overexpression of mNaChBacMut did not alter the action potential threshold (**f**, $P = 0.9$) and the rheobase current (**g**, $P = 0.8$). The numbers of recorded neurons are indicated on the bars. All data are expressed as mean \pm s.e.m.



Extended Data Figure 7 | Postnatal expression of mNaChBac and Kir2.1 using Flpo and F-FLEX switch.

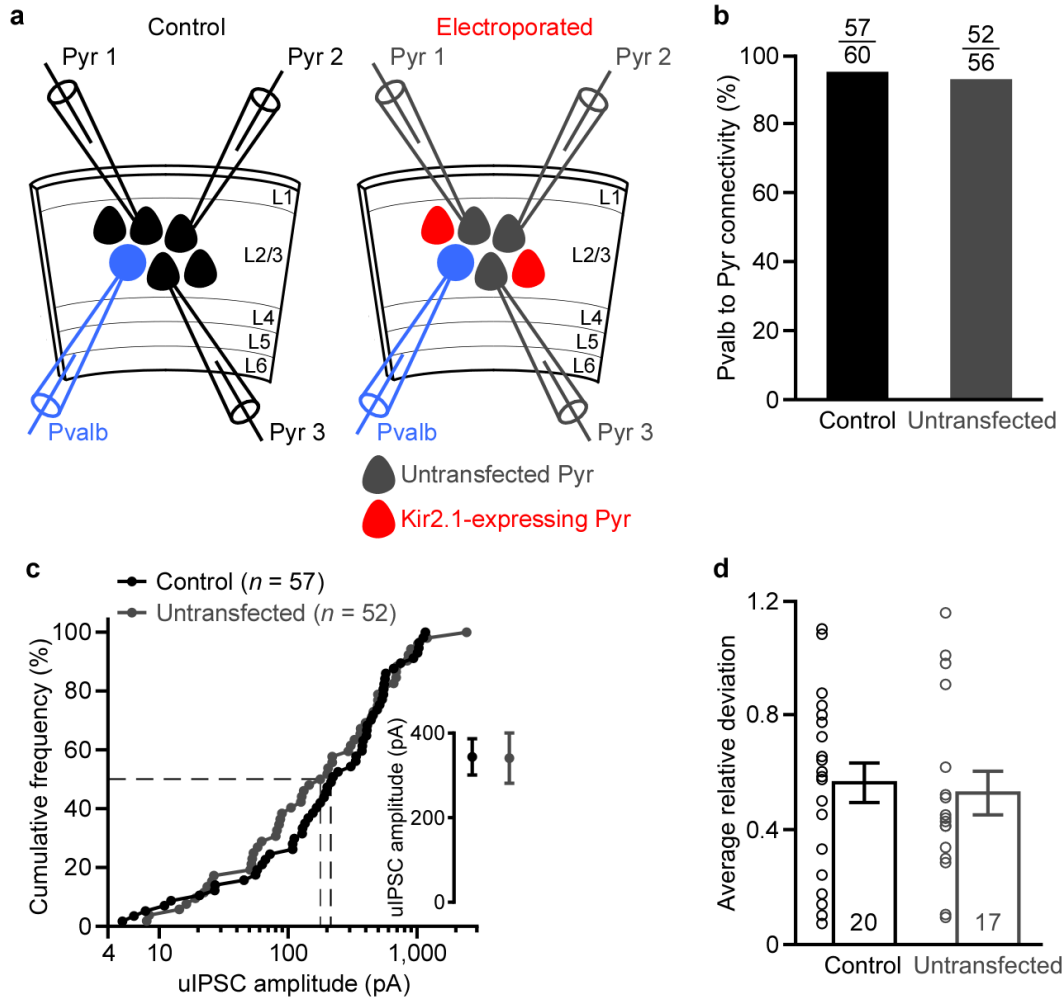
a, Constitutive overexpression of mNaChBac causes a neuronal migration defect. mNaChBac or mNaChBacMut was overexpressed in a subset of pyramidal cells by *in utero* electroporation of pCAG-mNaChBac-T2A-tdTomato or pCAG-mNaChBacMut-T2A-tdTomato, respectively, on embryonic day 15.5 (E15.5). Representative fluorescent images of coronal sections of V1 obtained at postnatal day 16 or 17 showing that mNaChBac-expressing neurons (left panels) resided not only in layer 2/3, but also in layers 4–6 ($n = 7$ mice), whereas mNaChBacMut-expressing neurons (right panels) are all located in layer 2/3 ($n = 5$ mice). Cortical layers are indicated on the right based on the DAPI staining pattern. **b**, Experimental procedures for conditional expression of mNaChBac or Kir2.1 in a subset of layer 2/3 pyramidal cells. Left, plasmids pAAV-EF1 α -F-FLEX-mNaChBac-T2A-tdTomato or pAAV-EF1 α -F-FLEX-Kir2.1-T2A-tdTomato together with pCAG-EGFP were electroporated *in utero* into V1 on embryonic day 15.5. Successful transfection is indicated by the expression of EGFP. Middle, AAV-hSynapsin-Flpo was injected postnatally into V1. Right, only those neurons that were transfected with either pAAV-EF1 α -F-FLEX-mNaChBac-T2A-tdTomato

or pAAV-EF1 α -F-FLEX-Kir2.1-T2A-tdTomato and infected with AAV-hSynapsin-Flpo expressed mNaChBac-T2A-tdTomato or Kir2.1-T2A-tdTomato, respectively. **c**, Representative fluorescent images of coronal sections of V1 obtained at postnatal day 16 showing that without injection of AAV-hSynapsin-Flpo transfected neurons did not express mNaChBac-T2A-tdTomato (left panels, $n = 2$ mice). The expression of mNaChBac-T2A-tdTomato in transfected neurons was turned on by injection of AAV-hSynapsin-Flpo. These neurons were all properly located in layer 2/3 (right panels, $n = 7$ mice). Cortical layers are indicated on the right based on the DAPI staining pattern. **d**, Schematics of concurrent expression of mNaChBac or Kir2.1 in layer 2/3 pyramidal cells and Chr2 in Pvalb or Sst cells. Plasmids pAAV-EF1 α -F-FLEX-mNaChBac-T2A-tdTomato or pAAV-EF1 α -F-FLEX-Kir2.1-T2A-tdTomato were electroporated *in utero* together with pCAG-EGFP into V1 of *Pvalb-ires-Cre* or *Sst-ires-Cre* mice on embryonic day 15.5. AAV-EF1 α -DIO-hChr2(H134R)-EYFP and AAV-hSynapsin-Flpo were injected postnatally into V1. Chr2 was conditionally expressed in Pvalb or Sst cells, whereas mNaChBac or Kir2.1 was conditionally expressed in a subset of layer 2/3 pyramidal cells.



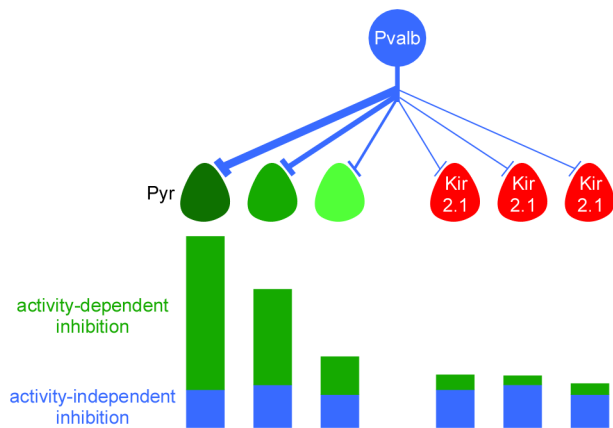
Extended Data Figure 8 | A Flpo recombinase-mediated FLEX (F-FLEX) switch for conditional gene expression. **a**, DNA sequence of the F-FLEX switch cassette. The first *F14* site and *Frt* site were constructed in the forward direction and were separated by a 50-base-pair linker. The second *F14* site and *Frt* site were constructed in the reverse direction and were separated by another 50-base-pair linker. Multiple cloning sites were inserted between the first *Frt* site and the second *F14* site. **b**, Principle of F-FLEX switch. The gene of interest is inserted between the first *Frt* site and the second *F14* site of the F-FLEX switch cassette in an inverted orientation, and is driven by an *EF1 α* promoter. Flpo-recombinase-mediated recombination first occurs between the two *F14* sites or the two *Frt* sites that are in the opposite direction, leading to a reversible inversion of the inverted gene of interest. Flpo-mediated recombination then occurs between the two *F14* sites or the two *Frt* sites that are now in the same direction, excising the *Frt* site or the *F14* site between them, respectively. The resulting construct contains only one *F14* site and one *Frt* site, and the gene of

interest is permanently locked in the forward orientation. **c**, Flpo turns on F-FLEX switch. HEK cells were transfected with (1) Flpo, (2) F-FLEX-mNaChBac-T2A-tdTomato, (3) Flpo and F-FLEX-mNaChBac-T2A-tdTomato or (4) Cre and F-FLEX-mNaChBac-T2A-tdTomato. EGFP was co-transfected to monitor the transfection. There was no leaky expression of mNaChBac-T2A-tdTomato in the absence of Flpo. mNaChBac-T2A-tdTomato expression was switched on by the expression of Flpo, but not by Cre. Similar results were obtained with other F-FLEX constructs ($n = 5$). **d**, Flpo does not turn on Cre-dependent DIO switch⁴⁶. HEK cells were transfected with (1) Cre, (2) DIO-hChr2(H134R)-EYFP, (3) Cre and DIO-hChr2(H134R)-EYFP or (4) Flpo and DIO-hChr2(H134R)-EYFP. mRFP was co-transfected to monitor the transfection. There was no leaky expression of hChr2(H134R)-EYFP in the absence of Cre. hChr2(H134R)-EYFP expression was switched on by the expression of Cre, but not by Flpo. Similar results were obtained with other DIO constructs ($n = 2$).



Extended Data Figure 9 | Overexpression of Kir2.1 in a small subset of layer 2/3 pyramidal cells does not affect Pvalb-cell-mediated inhibition onto untransfected pyramidal cells. **a**, Schematic of experiments. Unitary connection from a Pvalb cell onto nearby layer 2/3 pyramidal cells in control mice (left) and onto untransfected pyramidal cells in mice that were electroporated *in utero* with pCAG-Kir2.1-T2A-tdTomato (right). **b**, Connectivity rates from Pvalb cells to layer 2/3 pyramidal cells in control

mice (95%, 57 out of 60) and to untransfected pyramidal cells in electroporated mice (93%, 52 out of 56) are similar ($P = 0.7$). **c**, Cumulative frequencies for uIPSC amplitudes (control: $n = 57$, median, 224.0 pA; untransfected: $n = 52$, median, 190.4 pA; $P = 0.5$). Inset, mean \pm s.e.m. **d**, Summary graph for the average relative deviations of uIPSCs from 20 and 17 similar experiments as in **a**. Bars, mean \pm s.e.m. ($P = 0.6$).



Extended Data Figure 10 | A model for inter-cell variability of Pvalb-cell-mediated inhibition. Schematic illustration of how pyramidal cell activity regulates the inter-cell variability of Pvalb-cell-mediated inhibition. Left, pyramidal cells with different activity levels (dark and light colours indicate high and low activity, respectively) receive different amounts of Pvalb-cell-mediated inhibition (long and short bars indicate more or less inhibition, respectively). Inhibition consists of an activity-dependent component (green bars) and an activity-independent component (blue bars). The activity-dependent component is positively regulated by the pyramidal cell activity and varies accordingly, whereas the activity-independent component is similar across neurons. Right, when the activity of pyramidal cells is suppressed by overexpression of Kir2.1, the activity-dependent component is diminished and the remaining inhibition is largely the activity-independent component. This flooring effect reduces the variability of uIPSC amplitudes among Kir2.1-expressing neurons.